Coronal mass ejections and space weather

Nat Gopalswamy

NASA Goddard Space Flight Center, Greenbelt, Maryland, USA
E-mail: Nat.Gopalswamy@nasa.gov

Solar energetic particles (SEPs) and geomagnetic storms are the two primary space weather consequences of coronal mass ejections (CMEs) and their interplanetary counterparts (ICMEs). I summarize the observed properties of CMEs and ICMEs, paying particular attention to those properties that determine the ability of CMEs in causing space weather. Then I provide observational details of two the central issues: (i) for producing geomagnetic storms, the solar source location and kinematics along with the magnetic field structure and intensity are important, and (ii) for SEPs, the shock-driving ability of CMEs, the Alfven speed in the ambient medium, and the connectivity to Earth are crucial parameters.

1   Introduction

Space weather can be described as the physical conditions in space that affects human technology in space and on the ground as well as life on Earth in a number of ways including satellite drag, satellite sensor degradation, effects of geomagnetically induced currents on the power grid and pipelines, radiation threat to crews of high-flying aircraft and astronauts, high-frequency communication outages in the polar regions (see articles in Song *et al*., 2001). Space weather is mainly caused by the Sun because of the variability in its mass and photon emissions on various time scales. The electromagnetic emission consists of the quasi-steady irradiance and flares. While the long-term variability in photon emission may be related to climate effects, the short-term variation (solar flares) affects Earth's ionosphere resulting in a number of communication problems. The ionization is increased by the flash of enhanced X-ray and EUV emission during flares. The mass emission from the Sun has three components: the ubiquitous solar wind, coronal mass ejections (CMEs), and solar energetic particles (SEPs). CMEs and the solar wind carry the coronal magnetic field into the heliosphere. CMEs propagate into the solar wind and drive shocks; the shocks accelerate SEPs. Flares also accelerate particles, but generally over shorter duration and to lower intensity levels. When CMEs arrive at Earth, they interact with Earth's magnetosphere causing geomagnetic storms, which have multitude of effects from the magnetosphere to the ground. This paper discusses two main aspects of CMEs related to space weather: SEPs and geomagnetic storms (Gosling, 1993; Reames, 1999). Geomagnetic storms were known for a long time before the discovery of CMEs. Even Carrington (1860) suspected that the flare he discovered on 1859 September 1,
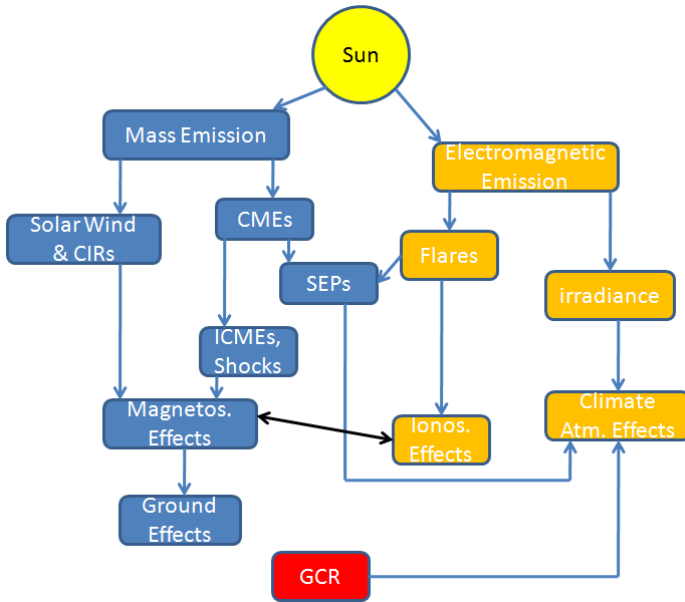
Fig. 1. The two primary outputs (mass and electromagnetic emissions) from the Sun, whose variability affects the heliosphere in general and the geospace in particular. The mass emission manifests as the solar wind, coronal mass ejections (CMEs), and solar energetic particles. CMEs and the solar wind also carry magnetic fields with them. The galactic cosmic rays (GCRs) enter the heliosphere from outside and interact with the solar wind and CMEs. Neutral matter also enters the heliosphere, gets ionized and accelerated as anomalous cosmic rays (not shown).

may have something to do with the huge geomagnetic storm that occurred the next day (but decided against the association). SEPs were detected in 1942 and reported in 1946 (Forbush, 1946). An interesting discussion on the development of the term Space Weather can be found in Kane (2006).

   Figure 1 illustrates how the two primary outputs (mass and electromagnetic emissions) from the Sun, whose variability affects the heliosphere in general and the geospace in particular. Both the solar wind and CMEs cause geomagnetic storms, but the CMEs are the primary cause of SEPs. In addition to being the source of SEPs, CMEs also deflect the galactic cosmic rays (GCRs) that enter the heliosphere from outside, thus producing the well known Forbush effect. Neutral matter also enters the heliosphere, gets ionized and accelerated as anomalous cosmic rays (not shown). This article focuses on issues related to CMEs. Interaction between fast and slow solar wind streams form corotating interaction regions (CIRs) that also can cause geomagnetic storms of lower intensity and accelerate particles at several AU from the Sun; these will not be discussed here.

   Section 2 summarizes the basic properties of CMEs derived from remote-sensing observations by coronagraphs, in particular the Large Angle and Spectrometric Coro-

nagraph (LASCO) on board the Solar and Heliospheric Observatory (SOHO). The SOHO mission has observed more than 13,000 CMEs during cycle 23, which form the basis of the description provided here. Section 3 describes CMEs in the interplanetary (IP) medium (ICMEs for short), mostly observed in the near-Earth space by spacecraft such as Wind and the Advanced Composition Explorer (ACE), emphasizing on the connection between CMEs and ICMEs. Section 4 presents CMEs as a source of geomagnetic storms and how the ICME properties such as speed and magnetic content influence the intensity of the resulting geomagnetic storms. Section 5 presents the association between CMEs and SEP events, especially those relevant to space weather. Finally, Section 6 summarizes the article.

2 Properties of Coronal Mass Ejections

CMEs are magnetized plasma structures that erupt from closed field regions on the Sun (active regions and quiescent filament regions) and propagate into the heliosphere. Recent reviews on CMEs can be found in Gopalswamy (2004, 2006a, b), Kahler (2006), Kunow *et al*. (2006). In white-light observations, CMEs appear as large-scale features moving away from the Sun. Coronagraphs image the CMEs in Thomson-scattered photospheric light, by blocking the direct sunlight using an occulting disk. Therefore, details of the source region are usually obtained using non-coronagraphic observations such as in X-rays, EUV, microwaves, and H-alpha (Gopalswamy, 1999; Hudson and Cliver, 2001). Photospheric magnetograms show that the CME source regions have generally enhanced magnetic fields (consisting of opposite polarity patches) compared to the quiet Sun regions. Magnetic field lines extending into the corona are inferred to be connecting the two polarities. It is believed that free energy can be stored in the coronal field lines, which are then released in the form of CMEs.

2.1 Morphology

Figure 2 shows two CMEs imaged by SOHO/LASCO. The first CME (2001 December 20) shows the three-part structure of CMEs: the core, void, and frontal structure (Illing and Hundhausen, 1986). The void is supposed to be a region of high magnetic field. In some CMEs the void region appears to have a flux rope structure (Chen *et al*., 1997). In the difference images one can see perturbations around the CME and the deflection of a nearby streamer. The second event (2003 November 18) CME, on the other hand, shows just a single feature. However, the difference image shows a faint feature surrounding the CME, which is likely to be the sheath of the shock driven by the CME. While shocks are readily inferred from radio-burst observations, it is generally difficult to identify them from white-light observations (Sheeley *et al*., 2000; Vourlidas *et al*., 2003). The second CME in Fig. 2 originated from close to the disk center contrary to the first event, which erupted from close to the southeast limb. The viewing angle can significantly affect the appearance of CMEs. The bright core of the CME is the eruptive prominence (also known as eruptive filament when happening on the disk), that lies along and above the photospheric neutral line in the pre-eruption phase.
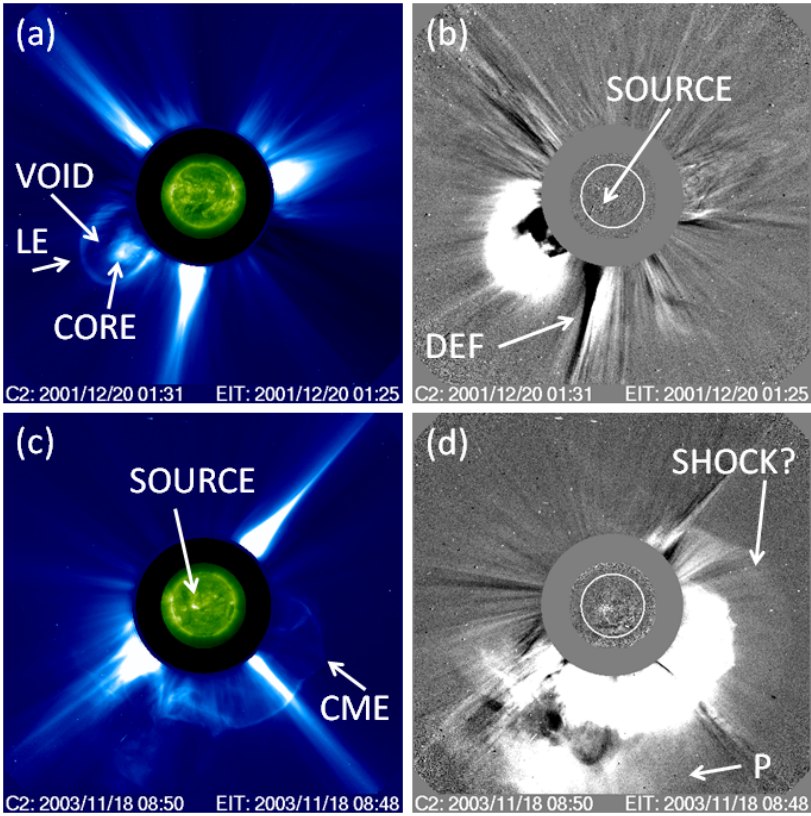
Fig. 2. CME morphology as illustrated using two CMEs, one originating from close to the limb (top panels) and the other from close to the disk center (bottom panels). The left images are direct images with SOHO's Extreme-ultraviolet imaging telescope (EIT) images superposed on the LASCO images. The source locations of the eruptions are seen as compact bright features in the EIT images (SOURCE). The right images are difference images with the previous frames subtracted to see the changes taking place in the corona. The three-part structure is evident in the first CME (2001 December 20—(a, b)), while only a single structure is seen in the second (2003 November 18—(c, d)). The CME leading edge (LE) also known as the frontal structure is the outermost feature followed by a void region (also known as the cavity) and the prominence core. The difference images show perturbations around the CMEs. The dark regions in the difference images correspond to material depletion, which normally indicates the displacement of a structure between the two frames used. In the first CME, one can see streamer deflections (DEF) and in the second case, there seems to be a shock and the associated sheath surrounding the CME. A previous CME (P) is in progress when the second CME was ejected.

2.2 Physical properties

CMEs are multithermal plasmas containing coronal material at a temperature of $\sim$ a few $\times 10^6$ K in the frontal structure and cavity. The prominence core is at a temperature $\sim$8000 K in the early phases. The prominence gets heated as time progresses and may contain plasma of multiple temperatures. Heated plasma ($\sim 10^7$ K) is also

thought to be injected into CME structures, observed as material with high charge states at 1 AU (Henke *et al.*, 2001; Reinard, 2005; Aguilar-Rodriguez *et al.*, 2006). The density in the frontal structure of CMEs close to the Sun is estimated to be in the range 10^{8-9} cm^{-3} and is expected to decrease as the CME expands into the interplanetary space. The prominence is denser by three orders of magnitude, which is the reason it appears as the brightest in white light images. The void region is inferred to have a lower density compared to the frontal structure. Direct measurement of the magnetic field strength in CMEs has not been possible yet. However, magnetic field in prominences (before eruption) has been measured, which ranges from a few G to $\sim$100 G. Moving type IV radio bursts produced by energetic electrons gyrating in CME structures or producing plasma emission imply that the magnetic field strength should be in the range 2–10 G in CMEs (Dulk and McLean, 1978; Gopalswamy and Kundu, 1989; Bastian *et al.*, 2001), which overlaps with prominence field strengths. The electrons must be trapped in the void region of the CMEs, which is thought to be a flux rope. The frontal structure is of higher density and lower magnetic field strength compared to the void region.

2.3   Kinematic properties

Speed, angular width, and acceleration are considered to be the basic attributes of a CME, measured from a series of images taken during an eruption. CME properties summarized here were obtained from the SOHO data. The speed measured in the sky plane varies from $\sim$20 km/s to >3000 km/s. The speed distribution of more than 10,000 CMEs observed during solar cycle 23 (see Fig. 3) has an average value of $\sim$470 km/s. The highest speed recorded is $\sim$3387 km/s for a CME on 2004 November 10. The CME width (W) ranges from <5° to 360°. Widths down to $\sim$2° are measured, but many such narrow CMEs might have been missed especially during the solar maximum. CMEs with $W = 360°$ (apparent) are the halo CMEs (Howard *et al.*, 1982). The true width of halos ($W = 360°$) and partial halos ($120° < W < 360°$) are unknown, so the average width ($\sim$54°) in Fig. 3(b) includes only CMEs narrower than 120°. Halo CMEs constitute only $\sim$3% of all CMEs, while CMEs with $W \geq 120°$ account for $\sim$11%. Although discovered in the Solwind era, the importance of halo CMEs for space weather was recognized only in the SOHO era (Webb *et al.*, 2000; Zhao and Webb, 2003; Gopalswamy *et al.*, 2007). Halo CMEs are more energetic than average CMEs (average speed $\sim$1000 km/s) and when they originate on the frontside of the Sun, they can directly impact Earth (see Section 3.3).

The above values of speed and width are consistent with those obtained from all the previous coronagraphs (see e.g., Howard *et al.*, 1985; Hundhausen, 1997; Gopalswamy, 2004; Kahler, 2006). In many cases the speed changes within the coronagraphic field of view because CMEs are subject to propelling and retarding forces. The distribution of measured accelerations in Fig. 3(c) shows that on the average, the acceleration is almost zero. However, CME acceleration within the coronagraphic field of view is speed-dependent (Gopalswamy *et al.*, 2001a; Vršnak *et al.*, 2004; Yashiro *et al.*, 2004; Gopalswamy, 2006a). CMEs faster (slower) than the solar wind accelerate (decelerate), while those moving at the solar wind speed show little acceleration. The sky-plane measurements shown in Fig. 3(a–c) are subject to projec-
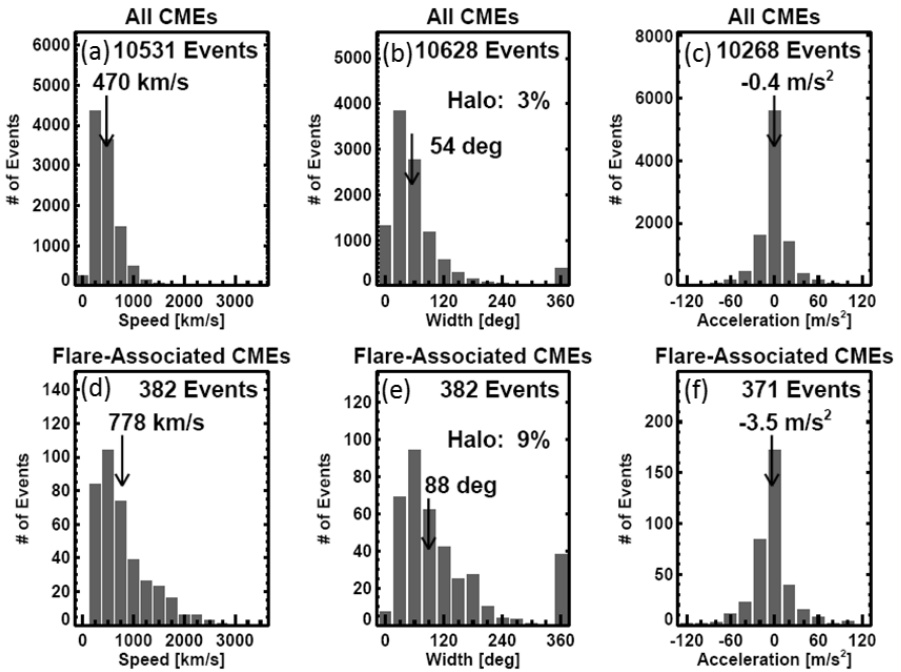
Fig. 3. Distributions of speed, width, and acceleration of all CMEs during 1996–2005 (top) and a subset of CMEs that originated within 30° from the limb (bottom). The CMEs in the bottom panel were chosen based on their association with flares above C3.0 class.

tion effects, which can be avoided when CMEs occurring at large central meridian distance (CMD) ($60° \leq \text{CMD} < 90°$) are considered. The speed, width, and acceleration distributions of the subset of CMEs are shown in Fig. 3(d–f). The average speed and width of the limb CMEs are higher and the acceleration is more negative. For definitiveness, we selected only CMEs associated with flares of X-ray importance C3.0 and higher, which might have contributed to the higher average speed of CMEs, in addition to the fact that the limb CMEs are not subject to projection effects.

2.4 Mass and kinetic energy

The mass content of CMEs ranges from $\sim 10^{12}$ g to $> 10^{16}$ g, wider CMEs being more massive. The mass is estimated from coronagraphic images as the excess mass above the pre-event corona. The mass below the occulting disk is not included. Each CME is assigned a single mass value, which is the mass attained in the outer corona after an initial increase with time, similar to the CME width (Vourlidas *et al.*, 2002). The average value of CME mass is $\sim 4 \times 10^{14}$ g. The CME kinetic energy ranges from $\sim 10^{27}$ erg to $> 10^{33}$ erg (average $\sim 5.4 \times 10^{29}$ erg), making CMEs the most energetic phenomenon in the heliosphere (Gopalswamy, 2004).
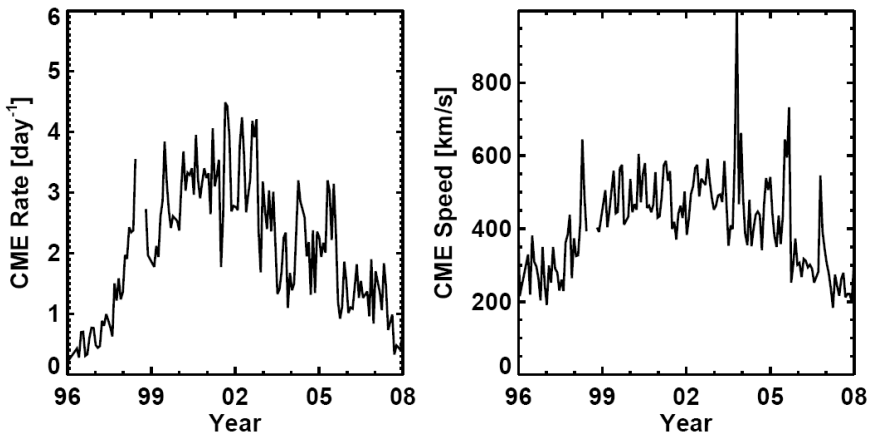
Fig. 4.   CME rate (per day) and speed averaged over Carrington rotation periods. CMEs with width
≥30° are considered. The large spikes in the speed plot are due to CMEs from super active regions
that produced energetic CMEs in quick succession. Note that the CME rate varies over a factor of 10
from solar minimum to maximum, while the mean speed increases by a factor ∼2. (Updated from
Gopalswamy *et al.* (2006).)

2.5   CME rate

CMEs are rather frequent: the daily CME rate averaged over Carrington rotation
periods ranges from <0.5 per day (solar minimum) to >6 CMEs per day (solar max-
imum). It is not uncommon that more than a dozen CMEs occur on individual days
(Gopalswamy *et al.*, 2003a). The CME daily rate also shows solar-cycle variation
with notable deviations from that of the sunspot number. CMEs originate from closed
magnetic field regions, which may or may not have sunspots. For example, quiescent
filament regions have no sunspots, but can produce CMEs. In fact, the high-latitude
(>60°) CMEs associated with polar-crown filaments can contribute significantly to
the total CME rate during solar maxima (Hundhausen, 1993; Gopalswamy *et al.*,
2003b). Figure 4 shows the daily CME rate and speed averaged over Carrington rota-
tion periods including only those CMEs with width ≥30°. This restriction eliminates
the non-uniformity in identifying weak and narrow CMEs (Yashiro *et al.*, 2008a). The
rate jumps by an order of magnitude from the minimum to the maximum phase of the
solar cycle. CMEs also seem to be more energetic during solar maxima: the average
speed of CMEs increases by a factor of >2 from ∼250 km/s during solar minimum
to ∼550 km/s during solar maximum. The large spikes in the speed plot correspond
to energetic CMEs from some super active regions that were prolific producers of
CMEs and flares (Gopalswamy *et al.*, 2006).

2.6   Associated phenomena

CMEs are associated with a number of phenomena occurring in the chromo-
sphere, corona, and interplanetary space. Flares, shocks, radio bursts, SEP events,
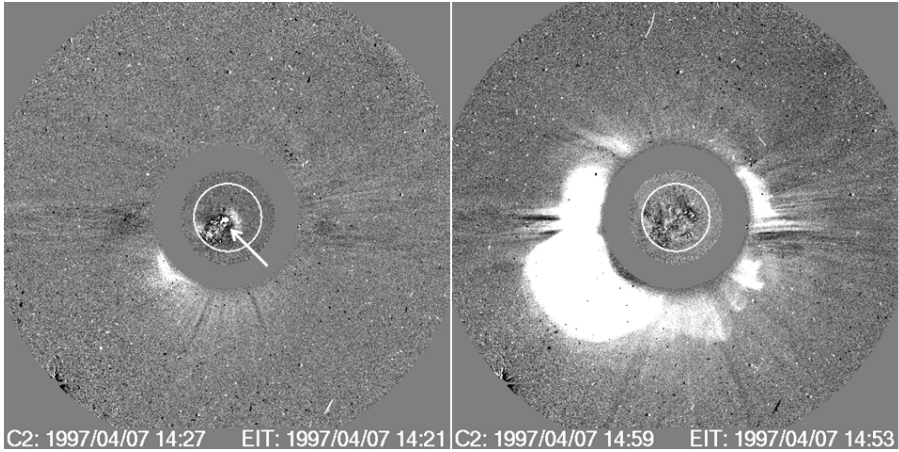ICMEs, and geomagnetic storms are all associated with CMEs. Most of these phe-

Fig. 5. Example showing how CMEs are related to the disk activity using EUV and white light difference
    images from SOHO. The arrow points to the location of eruption. The CME occurred on 1997 April 07.

nomena are observed in H-alpha, soft X-rays, EUV, radio, hard X-rays, and gamma
rays in images and/or spectra. Radio bursts of type II (produced by nonthermal elec-
trons accelerated in shocks) and type IV (produced by nonthermal electrons trapped
in moving magnetic structures), are closely related to CMEs. H-alpha flare ribbons
(Munro *et al.*, 1979), coronal dimming (Rust, 1983; Hudson and Webb, 1997; Zarro
et al., 1999; Thompson *et al.*, 2000), EUV wave transients (Biesecker *et al.*, 2002;
Cliver *et al.*, 2005; Chen, 2006; Veronig *et al.*, 2006) and post-eruption arcades
(Kahler, 1977; Tripathi *et al.*, 2004) are the disk signatures routinely used in iden-
tifying the source regions of CMEs on the Sun. Figure 5 illustrates how the disk
activity in EUV relates to the white-light CME. Changes in the corona are usually
best observed in difference images obtained by subtracting a previous frame from a
given frame. In Fig. 5, the EUV difference image at 14:21 UT shows a large-scale
disturbance originating from a location pointed by the arrow. The same disturbance
can be seen in the LASCO difference image taken 6 minutes later. The EUV distur-
bance can be seen over the entire solar disk in the next image at 14:53 UT and the
CME has already expanded to cover most of the coronagraph field of view. The EUV
disturbance is thought to be a wave in the corona surrounding the CME (Neupert,
1989; Thompson *et al.*, 1999); the wave, on occasions becomes a shock resulting in
a type II radio burst (Cliver *et al.*, 1999; Gopalswamy, 2006d). The EUV waves are
also observed in the chromosphere as Moreton waves (Moreton, 1960; Narukage *et
al.*, 2002; Warmuth *et al.*, 2005).

2.6.1 CMEs eruptive prominences

Prominence eruptions are known from the late 1800s from the scientific obser-
vations of Secchi and de la Rue (see, e.g., Tandberg-Hanssen, 1995) and recognized
as mass eruptions from the Sun. After the discovery of white light CMEs (see e.g.,
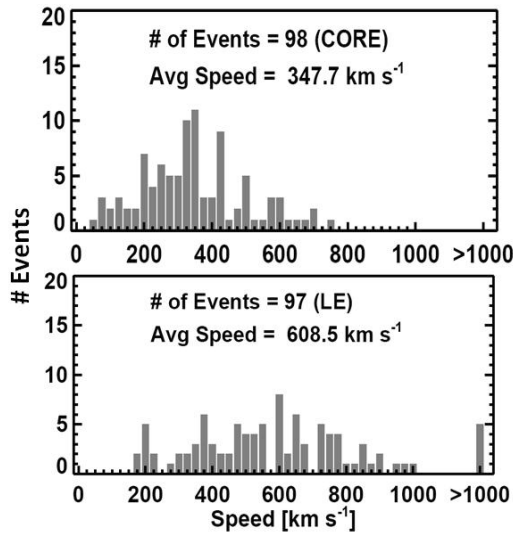
Fig. 6.   Speed distributions of the leading edge and prominence core of CMEs observed in the SOHO/LASCO field of view. The average leading edge speed is much higher (~609 km/s) than that of the core (348 km/s). (Adapted from Gopalswamy *et al.* (2003c). Reproduced by permission of the AAS.)

Koomen *et al.*, 1974), the eruptive prominence has been found to be the inner core of CMEs (see, e.g., House *et al.*, 1981; Gopalswamy *et al.*, 1998; Moore *et al.*, 2001) as illustrated in Fig. 2. When the eruption happens on the disk, dark filaments in H-alpha erupt and disappear. Filaments are the same as prominences but observed on the disk. The eruptive prominence is an integral part of an eruption, with a close correspondence between the onset times (Gopalswamy *et al.*, 2003c). CMEs selected on the basis of their association with eruptive prominences provide the true distribution of CME speeds because these CMEs are not subject to projection effects. Figure 6 shows the speed distributions of nearly 100 CMEs and their prominence cores as obtained from LASCO observations (Gopalswamy *et al.*, 2003c). The speed of the CME leading edge is nearly twice that of the associated prominence cores (609 km/s vs. 348 km/s). The lower speed of the prominences compared to the CME leading edge is considered as evidence that prominences may not be driving the CMEs (Hundhausen, 1999). However, some authors think that CMEs can be caused by prominence eruptions (Filippov, 1998). Prominence eruption is linked to the reconnection process between magnetic field that restrains the prominences and the newly emerging field in the CME source regions (Feynman and Martin, 1995; Shibata *et al.*, 1995). The average CME leading edge speed in Fig. 6 is similar to that of the limb population in Fig. 3(d), rather than that of the general population (Fig. 3(a)). This is because prominences indicate eruptions close to the limb, so the associated CMEs are subject to minimal projection effects (see also Burkepile *et al.*, 2004).

2.6.2 CMEs and flares

Like prominence eruptions, flares are also an integral part of CMEs. Flares associated with CMEs are known as eruptive flares as opposed to flares that are not associated with mass motion. Figure 7 illustrates a typical eruptive flare using H-alpha observations and the associated structures. One of the typical characteristics of an eruptive flare is the H-alpha ribbons (R1, R2 in Fig. 7) connected by post-eruption loops (PEL) straddling the polarity inversion line. When observed in EUV and X-rays, the ribbons + PEL are observed as post-eruption arcades (PEA). The ribbons correspond to the locations where energetic particles accelerated in the corona are supposed to deposit their energy thus exciting the H-alpha line. In a subset of the flare loops, precipitating energetic electrons produce hard X-ray emission, while trapped electrons produce microwave emission. The reconnection process that forms the PEA also forms a flux rope, which is ejected into the IP space as a CME. The axis of the flux rope (FR) is sketched in Fig. 7. The legs of the flux rope are thought to be anchored in a pair of dimming regions (D1, D2) usually observed in EUV images (see Fig. 7). The area of the flare ribbons defines the size of a flare in H-alpha referred to as optical importance of a flare. The soft X-ray flux from the PEA defines the X-ray importance of a flare. The X-ray importance is denoted by the letters X, M, C, B, and A from the largest (peak flux $>10^{-4}$ W m^{-2}) to smallest (peak flux $<10^{-7}$ W m^{-2}),
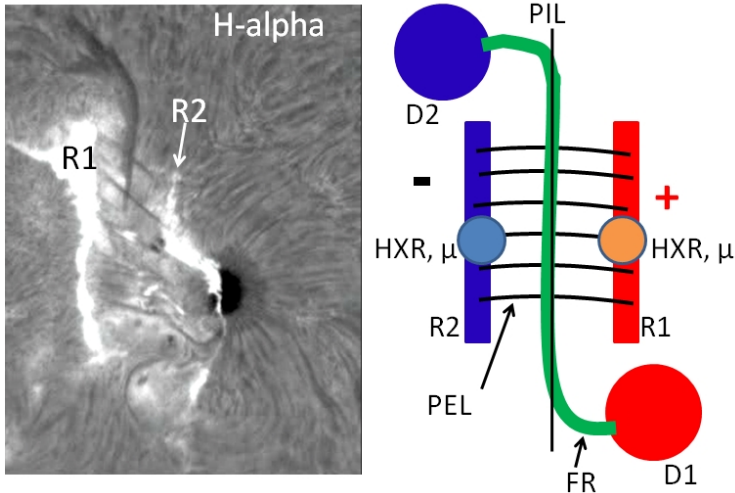

Fig. 7. (Left) H-alpha ribbons (R1, R2) with post-eruption loops (PEL) for a large-eruption that occurred on 2005 May 13. (Right) The eruption geometry sketched based on a number of observations from the photosphere to the interplanetary medium. In addition to the flare ribbons and post-eruption loops, the polarity inversion line (PIL) separating the positive and negative polarities in the active region, the dimming regions (D1, D2), and the sources of hard X-ray (HXR) and microwave (μ) emissions are also marked. The axis of a flux rope (FR) with its legs rooted in the dimming regions is also sketched. The flux rope and the PELs are formed by the reconnection process.
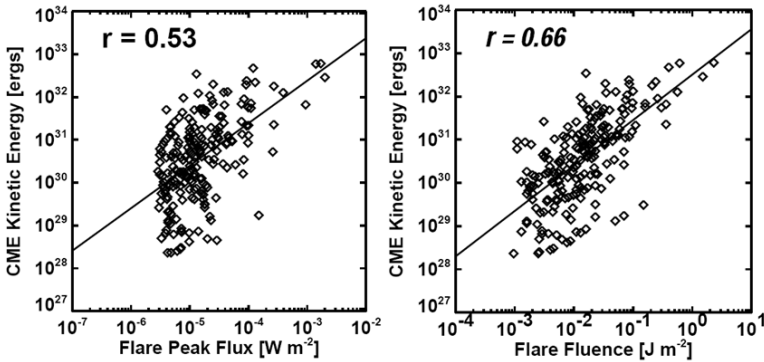
Fig. 8.   Scatter plot between CME kinetic energy and peak soft X-ray flux (left) and the fluence of the associated GOES soft X-ray flux. The correlation coefficients and the regression lines are also shown on the plots.

consecutive levels differing by an order of magnitude.

The sketch showed in Fig. 7 represents the top view of the standard eruption model known as the CSHKP (Carmichael, Sturrock, Hirayama, Kopp and Pneuman) model (see e.g., Švestka and Cliver, 1992; Hanaoka *et al.*, 1994; Gopalswamy, 2006c). The eruption geometry shown has some symmetry with the hard X-ray and microwave sources occupying the central location. The post-eruption arcade is the largest flare structure. The separation between the dimming regions is the largest structure, which represents the CME scale. The prominence core is supposed to be entrained at the bottom of the flux rope, which appears as the bright core in white light. The white light CME is actually the compressed coronal material that surrounds the flux rope. The symmetry suggested by the CSHKP model was not found in the statistical studies that investigated the spatial relationship between CME position angle and flare location in the pre-SOHO era: flare was thought to be located anywhere under the span of the CME (e.g., Harrison, 2006). These studies involved only a small number of CME-flare pairs. A recent investigation involving nearly 500 flare-CME pairs in the SOHO era found that the flare is typically located radially below the CME leading edge for limb CMEs (Yashiro *et al.*, 2008b). This finding calls for a closer flare-CME relationship as implied by the CSHKP eruption model and other observations connecting CME kinematics and soft X-ray flares (Zhang *et al.*, 2001).

How does the close spatial relationship between flares and CMEs figure in the energetics? Several authors have found varying degrees of correlation between CME speed and peak soft X-ray flux (Hundhausen, 1997; Moon *et al.*, 2002; Burkepile *et al.*, 2004; Vršnak *et al.*, 2005; Yeh *et al.*, 2005). Some used speed, others used CME kinetic energy. Not all took care of projection effects. Hundhausen (1997) reported a weak correlation ($r = 0.53$) between CME kinetic energy and peak soft X-ray flux of the associated flares for all the events observed by the Solar Maximum

Mission (SMM). Burkepile *et al.* (2004) reanalyzed the SMM data including only those CMEs originating close to the limb (to avoid projection effects) and found a better correlation ($r = 0.74$). Other attempts to correct for projection effects in fact worsened the correlation (Yeh *et al.*, 2005). Figure 8 shows another attempt to find the relation between flare and CME energies for a set of 379 SOHO CMEs that originated in the CMD interval $60°–90°$. The data set is similar to that of Burkepile *et al.* (2004) with minimal projection effects. It is clear that the resulting correlation coefficient is identical to that of Hundhausen (1997). However, the correlation between CME kinetic energy and flare fluence is much better ($r = 0.66$). It is possible that the higher correlation coefficient obtained by Burkepile *et al.* (2004) is due to a smaller sample size. The weaker correlation may not be entirely due to projection effects and may be related to the basic process by which the energy released in an eruption is partitioned between heating (soft X-ray flux) and mass motion (CME kinetic energy). For example, in confined flares the entire free energy goes into heating, with no mass motion in the radial direction. The overlying magnetic structure in the eruptive region may also influence the amount of mass ejected and hence the resulting CME kinetic energy.

It must be pointed out that only less than half of all flares are associated with CMEs. Is there any fundamental difference between flares with and without CMEs? Yashiro *et al.* (2006) studied two sets of flares one with and the other without CMEs. The number of flares as a function of peak X-ray flux, fluence, and duration in both sets followed power laws. Surprisingly, the power law index was >2 for flares without CMEs, while <2 for flares with CMEs. In flares without CMEs, the released energy seems to go entirely into heating, which suggests that tiny flares may contribute significantly to coronal heating as suggested by Hudson (1991). Another study found that flares without CMEs indicate a higher temperature (Kay *et al.*, 2003), which is consistent with the view that the entire released energy goes into heating.

2.6.3   CMEs and shocks

CMEs moving with super-Alfvenic speeds drive fast mode MHD shocks. The earliest indication of shocks in the corona is the metric type II radio bursts (Nelson and Melrose, 1985). Type II radio bursts are thought to be produced by nonthermal electrons accelerated in the shock front by the plasma emission mechanism (Langmuir waves generated by the nonthermal electrons get converted into electromagnetic radiation at the fundamental and harmonic of the local plasma frequency). Metric type II bursts (observed by ground based radio telescopes) start typically at 150 MHz and drift down to lower frequencies, corresponding to the heliocentric distances $<2–3R_o$ (solar radii) in the corona. Spaceborne radio instruments such as the Wind/WAVES experiment are needed to observe at frequencies below the ionospheric cutoff (~15 MHz). Type II radio bursts have been observed down to ~20 kHz, which corresponds to the plasma frequency in the vicinity of the observing spacecraft.

Figure 9 shows a type II radio burst and the associated CME, flare, and SEP activities. The continuous track of type II radio burst implies that the shock continuously accelerates electrons throughout the IP medium until the shock reaches the Wind spacecraft. Early in the event, type III bursts are produced, which are due to
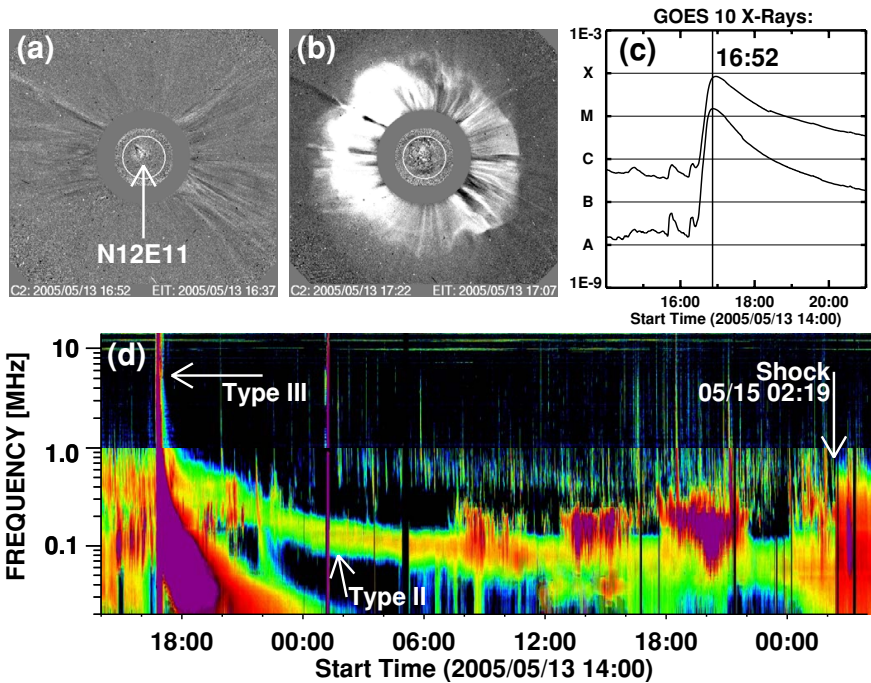
Fig. 9. A complete Sun-to-Earth event with (a) solar source near the disk center (N12E11), (b) a halo
CME, (c) a M-class GOES soft X-ray flare, (d) shock arrival as indicated by the SEP time profile, and
(d) an IP type II extending from the outer corona through the IP space to the observing spacecraft.

electrons accelerated in the flare site (Fig. 9(a, c)) located below the CME (Fig. 9(b)).
The SOHO coronagraphs track CMEs only up to $32R_o$ (the outer edge of the field
of view), whereas the Type II bursts can track the CME-driven shocks all the way to
Earth. Note that the type II radio emission occurs at ∼40 KHz when the shock arrives
at the spacecraft. When the Type II burst is at decameter-hectometric (DH) wave-
lengths (14–1 MHz), the shock is typically in the near-Sun interplanetary medium
(heliocentric distance in the range $3–10R_o$). When type II bursts are observed in the
DH and longer wavelengths, it is highly likely that the underlying shocks and CMEs
reach Earth (provided the CME source is close to the disk center). The lower the
frequency reached by a type II, the higher is the energy of the associated CME, im-
plying that such CMEs drive shocks throughout the inner heliosphere (Gopalswamy
et al., 2005a; Gopalswamy, 2006d). The GOES SEP intensity profiles (not shown)
reveal that SEPs are produced soon after the CME lifts off at the Sun with a sharp rise
when the shock arrives at the observing satellite. Such a rise is known as the ener-
getic storm particle (ESP) event because it coincides with the sudden commencement
of geomagnetic storms (see e.g., Cohen, 2006 for a review). SEPs will be discussed
in more detail in Section 5. Shocks are also observed in in-situ data marked by a

sudden jump in density, temperature, magnetic field, and flow speed. Shocks are important for space weather because they mark the first arrival of a CME-associated disturbance and the ESP event. Shocks also compress the magnetosphere making the magnetosphere shrink thereby exposing satellites in geostationary orbits to the solar wind.

3   Coronal Mass Ejections in the IP Medium

In the decade before the first detection of white-light CMEs, people contemplated about IP structures that are not too different from what are observed today. In particular, Parker (1957) concluded that "magnetic clouds may be ejected from a magnetic field with velocities as high as the Alfven wave velocity...". Gold (1962) had sketched (see Fig. 10) the "Idealized configuration in space, showing solar plasma cloud, the drawn-out field and the shock wave ahead". Koomen *et al*. (1974) found similarity between the Gold magnetic bottle and CMEs observed by OSO-7 coronagraph. While most CMEs fade to the background level within the coronagraphic field of view (below $\sim 32 R_o$), $\sim 10\%$ of them seem to go past the edge of the field of view and propagate as disturbances in the IP medium as envisaged by Gold (1962). The only difference between Gold's picture and modern picture is that the magnetic field of the plasma cloud should be in the form of a flux rope. The modern version of the Gold plasma cloud is known as ICMEs. Driver gas, ejecta, magnetic clouds (MCs) and flux ropes are other names for ICMEs. Although the Solar Terrestrial Relations Observatory (STEREO) mission is capable of observing CMEs over the entire Sun-
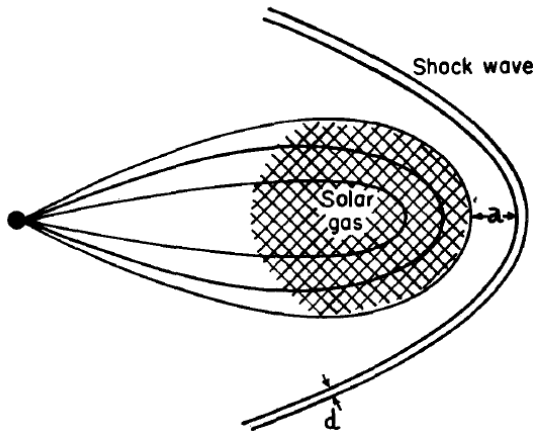

Fig. 10.   The spatial structure of an ICME as sketched by Gold (1962). Note the enormous size of the magnetized "plasma cloud" connected to the Sun and driving a shock that has a thickness d and stands ahead at a distance a from the cloud. This is pretty much the structure we know today, except for the flux-rope nature of the magnetized gas cloud. (With kind permission from Springer Science+Business Media: *Space Sci. Rev.*, Magnetic storms, **1**, 1962, 100–114, Gold, T.)

Earth distance (Harrison *et al.*, 2008), the current knowledge on ICMEs comes mainly from in situ observations.

3.1 ICME signatures

ICMEs are identified in a variety of ways: solar wind plasma signatures (temperature, plasma beta, flow speed), magnetic signatures (field strength, field rotation), compositional and charge state signatures, and particle (thermal and nonthermal) flux signatures (see Gosling, 1990; Neugebauer and Goldstein, 1997 for a review). Arrival of shocks at the spacecraft is also a good indicator of the impending ICME arrival except when the associated CME propagates at a large angle to the Sun-spacecraft line. In situ observations by the Helios and Pioneer Venus Orbiter spacecraft (at distances <1 AU), by Voyager spacecraft (at 10s of AU) and Ulysses spacecraft at high latitudes have shown that ICMEs are observed throughout the heliosphere (see e.g., Wang *et al.*, 2005 and references therein). Techniques such as IP scintillation observations and IP type II burst observations also provide information on parts of CMEs in the heliosphere (see e.g., Tokumaru *et al.*, 2007 and references therein).

Magnetic-field signatures are most useful to identify flux ropes: enhancement of the magnetic field magnitude, smooth rotation of the field along the trajectory of the observing spacecraft, and low proton temperature (or beta) (Burlaga *et al.*, 1981). MCs are also referred to as flux ropes, but the latter need not have low plasma beta. Bidirectional flux of thermal electrons, ions and energetic particles are signatures indicating that the legs of the ICME are connected to the solar corona. When the flux rope expands from near the Sun, the density and temperature decrease. Depressed proton temperature (with respect to an expected value—see Lopez and Freeman, 1986) is often used as a signature to identify intervals of ICMEs in solar wind data (Cane and Richardson, 2003; Neugebauer *et al.*, 2003; Elliott *et al.*, 2005). Charge state signatures include the enhancement of the average Fe charge state within the ICME (Lepri *et al.*, 2001), the density ratio of O^{7+} and O^{6+} ions (O^{7+}/O^{6+}—see Henke *et al.*, 2001; Reinard 2005; Aguilar-Rodriguez *et al.*, 2006), and the density ratio of helium ions to protons (N_α/N_p).

Figure 11 shows an ICME illustrated using plots of the magnetic field magnitude (B_t) and its Y and Z components (B_y, B_z), the solar wind bulk flow speed (V), proton temperature (T_p), and the alpha to proton density ratio (N_α/N_p) in GSE coordinates (from the ACE data). Also plotted are the expected solar wind proton temperature (T_{exp}) from Lopez and Freeman (1986). Ejecta intervals are those with T_p depressed significantly with respect to T_{exp}. In Fig. 11, T_p is depressed between 14:15 on 2005 January 16 to 06:30 on the next day. The ratio of helium density to proton density (N_α/N_p) is also enhanced during the ejecta interval. In addition, the magnetic field is enhanced, the B_z component shows rotation, and the B_y component points to the east throughout the ejecta interval. The white light CME responsible for the ICME was very fast (>2050 km/s) and originated close to the disk center (N16E04) on 2005 January 15 around 06:30 UT. The type II radio burst indicative of interplanetary shock is also shown in the figure. The shock was observed ahead of the ICME at 11 UT on 2005 January 16 in the in situ data. Nearly 200 such CME-ICME pairs have been identified during solar cycle 23, which helped assess the importance of
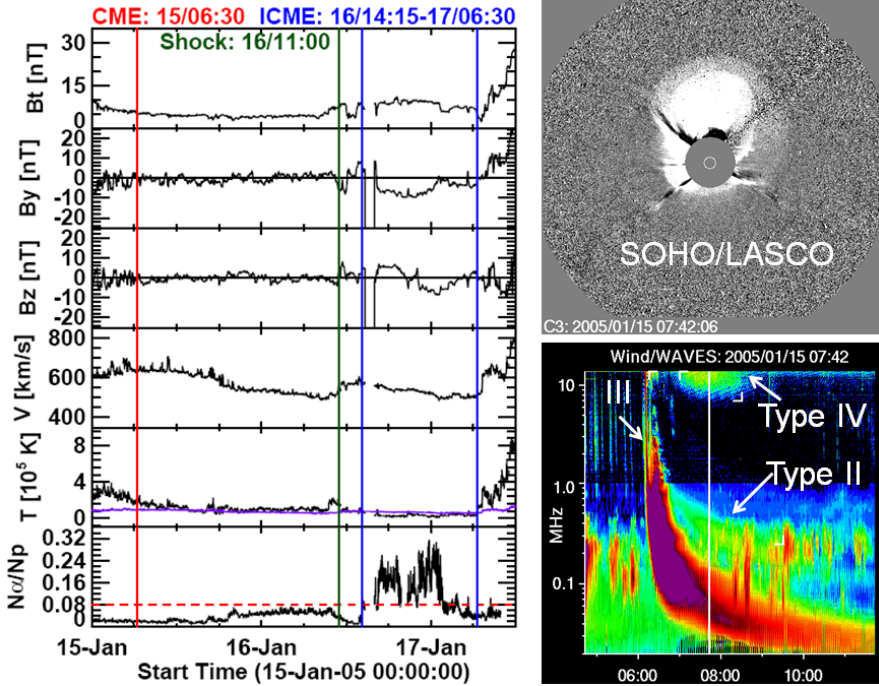
Fig. 11. Plots of the magnetic field magnitude (B_t) with its Y and Z components (B_y, B_z), the solar wind bulk flow speed (V), proton temperature (T), and the alpha to proton density ratio (N_α/N_p) in GSE coordinates (from the ACE data). The expected solar wind proton temperature (T_{exp}) from Lopez and Freeman (1986) is overlaid on the T plot. Ejecta intervals are those with T_p depressed significantly with respect to T_{exp}. The associated CME and the radio bursts are also shown.

CMEs in causing space weather effects.

3.2 Charge states in ICMEs

The solar wind ions maintain their chemical and charge state identity as they propagate into the IP medium because the expansion time scale is much larger than the ionization and recombination time scales. Thus the charge state of ions in the solar wind is a good indicator of the conditions in the corona where this time-scale inequality happens (also known as the freezing-in altitude). Since the source region of the CMEs is hotter than that of the normal solar wind, one expects higher charge states in ICMEs (Henke *et al.*, 2001; Reinard, 2005; Aguilar-Rodriguez *et al.*, 2006). In a study involving more than 150 ICMEs, Aguilar-Rodriguez *et al*. (2006) found that elements inside ICMEs have higher ionization states compared to those in the ambient solar wind. The required higher temperature in the CME source region can be traced to the flare plasma, which can exceed 10 MK: according to the standard model of CMEs associated with eruptive flares, the CME flux rope forms out of sheared active region field lines and the heated plasma from the reconnection region is injected into

the flux rope. As the flux rope expands, the ionization states corresponding to the flare plasma remain frozen. They also found that MCs possess the enhanced charge states more often than the non-cloud ejecta. Such a scenario is supported by the observed correlation between the flare size and charge state enhancement for eruptions close to the disk center (Reinard *et al.*, 2005). Off the disk center CMEs are likely to be observed by an observer along the Sun-Earth line as non-cloud ejecta, consistent with the observations of Aguilar-Rodriguez *et al.* (2006).

3.3 Solar sources of ICMEs

CMEs propagate radially outward from the Sun, so those directly impacting Earth must originate close to the disk center. It is well known that CMEs associated with MCs have their sources close to the disk center (see e.g., Gopalswamy *et al.*, 2000). The other extreme is the case of shocks arriving at Earth without discernible ejecta. These "driverless shocks" are associated with CMEs that travel approximately orthogonal to the Sun-Earth line, so their solar sources are expected to be close to the limb. Non-cloud ejecta must have their solar sources at intermediate longitudes. The source locations of the MCs, non-cloud ICMEs, and driverless shocks shown in Fig. 12 confirm the expected pattern: there is a heavy concentration of MC sources near the disk center, non-cloud ejecta sources are mostly at larger central meridian distances, and the driverless shock sources are mostly near the limb. There are significant exceptions to this pattern, especially for non-cloud ejecta and driverless shocks. Driverless shocks with their sources near the disk center are quite unexpected. A recent investigation revealed that the associated CMEs are deflected away from the Sun-
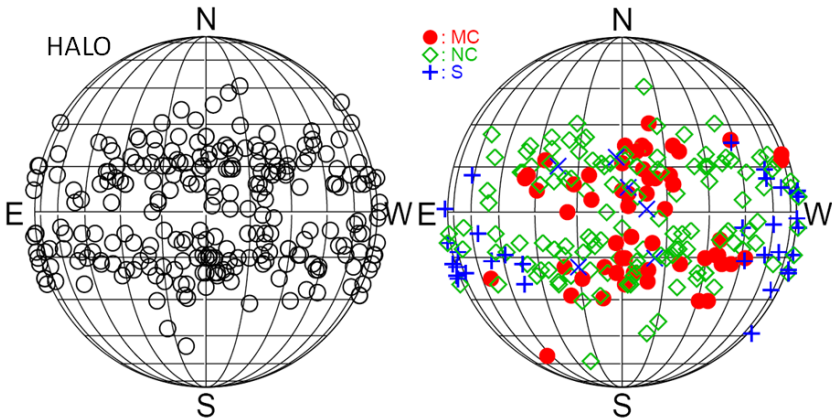

Fig. 12. (Left) Solar source locations of halo CMEs and (right) those of CMEs associated with magnetic clouds (filled circles), non-cloud ICMEs (NC, diamonds) and shocks without discernible drivers (plus and cross symbols). Although there are a few exceptions, the overall distribution of sources is similar in both cases. There is a heavy concentration of halo CME sources near the disk center. Similarly there is a heavy concentration of MC sources near the disk center. While there are many non-cloud ejecta from near the disk center, most of them are at large central meridian distances. The shocks are mostly near the limb, except for a handful of events near the disk center (cross symbols).

Earth line by coronal holes located in the vicinity of the eruption region (Gopalswamy *et al.*, 2008b), thus forcing the CMEs behave like limb events. Such deflections happened only during the declining phase of the solar cycle, when large low-latitude coronal holes occur frequently. A similar deflection is suspected in the case of non-cloud ICMEs with disk-center sources, but further investigation is needed to confirm this. This will also explain why some CMEs originating close to the disk center do not become MCs. According to the above geometrical argument, one would expect the central one third of ICMEs become MCs, assuming that most energetic CMEs have a width of ∼60°. In reality, the fraction of MCs changes with the phase of the solar cycle influenced heavily by the global field during solar minima (Riley *et al.*, 2006; Gopalswamy *et al.*, 2008a).

Figure 12 also compares the solar source locations of MCs, non-cloud ICMEs, and driverless shocks with those of halo CMEs. There is a heavy concentration of halo CME sources near the disk center, consistent with the result that ∼86% MCs are associated with halos or partial halos (Gopalswamy *et al.*, 2008a). Halos at larger CMD are expected to produce non-cloud ejecta at Earth. Finally, most of the limb halos produce driverless shocks. In the case of limb halos, the CME originates close to the limb, but the disturbance (most likely CME-driven shock) extends above the opposite limb because these CMEs are very energetic and expand rapidly to produce a signal above the opposite limb. As we noted before, CMEs associated with ICMEs are generally more energetic, similar to the halo CMEs.

3.4 Statistical properties of ICMEs

Figure 13 summarizes the properties of ICMEs separated into MCs and non-cloud events. For definitiveness we have included only those non-cloud ICMEs that drive shocks. The maximum magnetic field strength in the two types of ICMEs ranges from a few nT to several tens of nT. The average values are about three times that of the solar wind (∼5 nT), which confirms that enhanced magnetic field is an important ICME signature. The mean speeds of MCs (478 km/s) and non-cloud ICMEs (466 km/s) are also similar and only slightly larger than the typical slow solar wind speed (437 km/s—see Gopalswamy, 2006c). The average values of duration and proton thermal speed are smaller for MCs. The larger duration of non-cloud ICMEs may be due to the passage of the measuring spacecraft away from the nose of the flux rope. The MC duration implies a spatial scale of ∼0.3 AU for the thickness of the flux rope (see Lepping and Berdichevski, 2000; Gopalswamy, 2006c). The higher proton thermal speed may also indicate a spacecraft trajectory along the flanks of the ICME.

A compilation of ICME observations at various radial distances (R) made from many spacecraft (Helios-1 and 2, Pioneer Venus Orbiter, ACE, and Ulysses) reveal a rapid decline of density ($\sim R^{-2.4}$) and magnetic field ($\sim R^{-1.5}$) inside ICMEs compared to the solar wind (Wang *et al.*, 2005). The temperature, while smaller than in the solar wind, declines less rapidly ($\sim R^{-0.7}$). Extrapolating the 1-AU values of magnetic field, density and temperature in CMEs seem to agree with the expected values at the Sun.
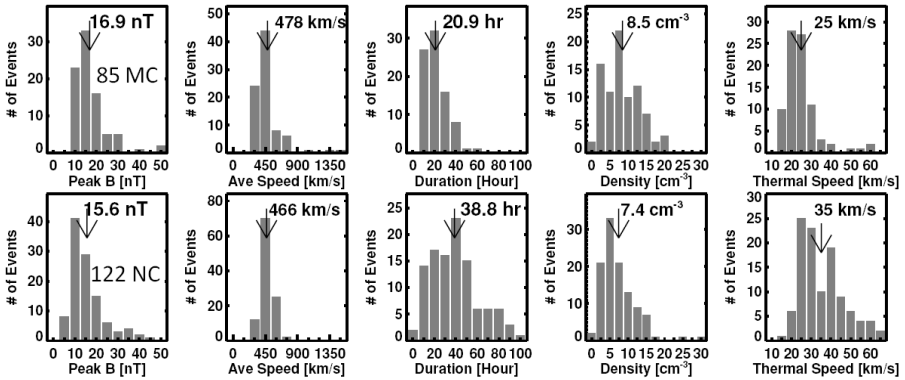
Fig. 13. Distributions of properties of MCs and non-cloud (NC) ICMEs observed during cycle 23: magnetic field strength, flow speed, duration, proton density and proton thermal speed. The average values of the distributions are marked on the plots. (With kind permission from Springer Science+Business Media: *Space Sci. Rev.*, Properties of interplanetary coronal mass ejections, **24**, 2006, 145–168, Gopalswamy, N., figure 4.)

3.4.1   CME and ICME speeds

Overall, the ICME speeds are not too different from the speed of the slow solar wind and the average speed of the general population of CMEs observed near the Sun. On the other hand the average speeds of CMEs associated with MCs and non-cloud ICMEs is close to 1000 km/s (Gopalswamy *et al.*, 2007). This is a direct consequence of the interaction between CMEs and the solar wind in the IP medium. Once a CME lifts off from the Sun, its subsequent evolution is determined by its interaction with its surroundings. After the propelling force ceases at a few solar radii, the interaction with the solar wind becomes the dominant force acting on the CME. This is normally described by the drag force, which depends on the flow properties of the ambient medium and the CME. The scatter plot in Fig. 14 shows how the speeds measured at the Sun and at 1 AU are related. While the CME speeds at the Sun varies from ∼100 km/s to >3000 km/s, the corresponding speeds at Earth range from ∼300 km/s to ∼1500 km/s. This is clearly an indication that slow CMEs at the Sun eventually accelerate, while the fast CMEs decelerate to produce the observed narrower range of speeds at Earth. In fact, there are only three ICMEs with speeds exceeding 1000 km/s. CMEs near the bisector do not change in speed because they are simply carried by the solar wind speed. Such a scatter plot was first obtained by Lindsay *et al.* (1999) using Helios and Pioneer Venus Orbiter data in the solar wind and coronagraphic observations near the Sun (Solar Maximum Mission and P-78 satellite data). They found a linear correlation. A reanalysis of the same data indicated that the relationship is not linear (Gopalswamy *et al.*, 2001b; Gopalswamy, 2002).

The interplanetary acceleration can be quantified using pairs of CMEs and ICMEs (Gopalswamy *et al.*, 2000, 2001b, 2005e): observational data devoid of projection
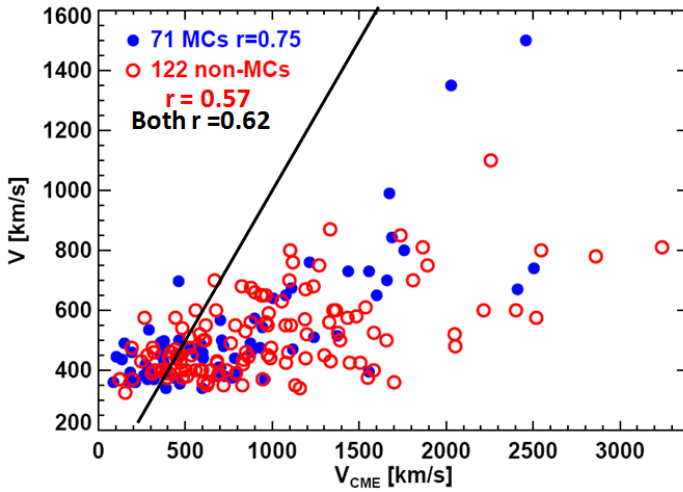
Fig. 14.   Scatter plot between CME speeds measured near the Sun (V_{CME}) and ICME speeds (V) mea-
sured at 1 AU. Magnetic cloud (MC) and non-cloud ICMEs are denoted by closed and open circles,
respectively. The solid line is the bisector. The correlation coefficient is significantly higher for
MCs ($r = 0.75$) than for non-cloud ICMEs ($r = 0.57$); the combined set has an intermediate value
($r = 0.62$). (Reprinted from *J. Atmos. Sol.-Terr. Phys.*, **70**, Gopalswamy, N., Solar connections of
geoeffective magnetic structures, 2078–2100, Copyright 2008, with permission from Elsevier.)
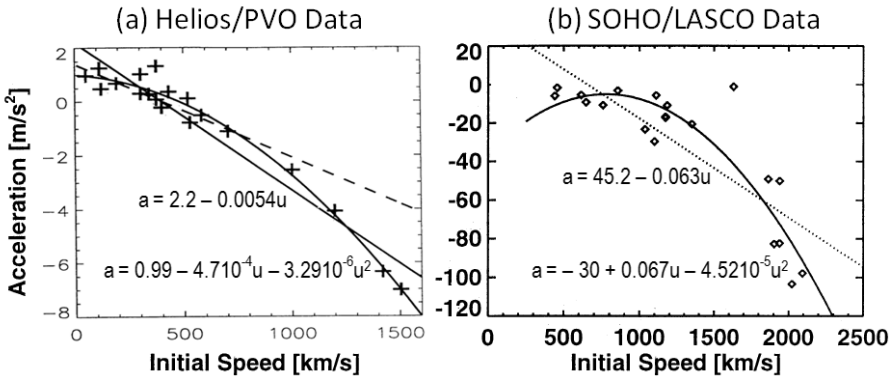

Fig. 15.   Dependence of acceleration as a function of initial speed of CMEs (a) over the Sun-Earth distance
(b) within the first 32 solar radii (from SOHO/LASCO).

effects indicate a linear relationship between acceleration (a) and the CME initial
speed (u): $a = 2.2 - 0.0054u$ or $a = -0.0054(u - 406)$, with a in m s^{-2} and u in
km/s (Gopalswamy *et al.*, 2001b). In this relation, the speed of 406 km/s corresponds
to the solar wind speed. From Fig. 15(a) we see that this linear relationship is quite

reasonable for speeds below $\sim$1000 km/s. At higher speeds, the quadratic relation seems to work better. In fact, within the coronagraphic field of view, the deceleration seems to be quadratic for limb CMEs that produce IP type II radio emission (see Fig. 15(b)).

While the acceleration profile is devoid of projection effects, its utility depends on obtaining the actual speed of CMEs in the Earth direction. Unfortunately, CMEs originating close to the disk center are the ones important for space weather, but they are subject to severe projection effects. At present there are two ways to eliminate projection effects. One is to fit the observed CME in the coronagraphic field of view to a cone and get the radial speed and width of the CME (Hundhausen *et al.*, 1994; Xie *et al.*, 2004; Michalek, 2006; Zhao, 2008). The other method is to obtain an empirical relation between the radial speed ($V_{\rm rad}$) and the expansion speed ($V_{\rm exp}$) of a set of CMEs occurring near the limb and then use the relation for CMEs for which the expansion speed can be measured. Dal Lago *et al.* (2003) obtained a relationship $V_{\rm rad} = 0.88 V_{\rm exp}$. One difficulty is that we do not know the actual width of halo CMEs, so the empirical relation leads to large uncertainties (Gopalswamy *et al.*, 2008e). Other possibilities include using a set of well observed CMEs when the separation between the STEREO spacecraft is $\sim$90° and/or when they are at 90° from the Sun-Earth line to validate the acceleration profiles and test their validity over the entire Sun-Earth distance.

3.5   Magnetic field structure

When a ICME is shock driving, one observes the following temporal ordering of structures: the shock, the sheath, and the ejecta in a typical time-series observation at 1 AU. In the case of MCs, the ejecta portion has a well defined structure with B_z showing a smooth rotation from north to south (NS) or south to north (SN) as illustrated in Fig. 16. This happens when the MC axis is close to the ecliptic ($Z = 0$ in GSE coordinates). B_z is the azimuthal component of the flux rope that defines the
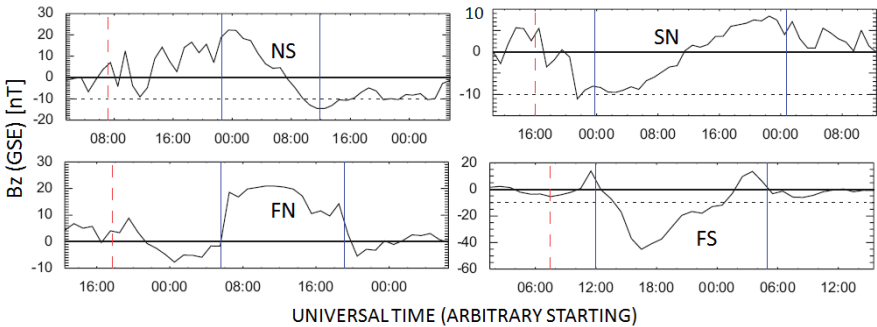

Fig. 16.   The four basic types of MCs defined based on the direction of the leading field from the B_z component in GSE coordinates: North-south (NS), south-north (SN), fully north (FN), and fully south (FS). The vertical dashed line denotes the shock. The MC interval is between the two vertical lines. The region between the shock and MC is the sheath region.

MCs. When the MC axis makes an angle $>45°$ to ecliptic, B_z is due to the axial field. For such high-inclination MCs, the azimuthal field (B_y) shows smooth rotation in the east-west direction. High-inclination MCs are known as unipolar MCs (Mulligan *et al.*, 1998) because the axis points fully to the north (FN) or south (FS) throughout the MC interval (see Fig. 16). Thus the SN, NS, FN, and FS MCs constitute the four basic types of flux ropes. Note that the each MC type can have two subtypes: the bipolar MCs can have their axes pointing to the east (SEN, NES) or west (SWN, NWS); the unipolar MCs can have their rotation from east to west (ESW, ENW) or west to east (WSE, WNE).

The flux rope types and their connection to the solar source regions have been extensively discussed in the literature (Bothmer and Schwenn, 1994; Mulligan *et al.*, 1998; Li and Luhmann, 2004; Yurchyshyn, 2008). In general, MCs have their axis parallel to the neutral line in the source active region on the Sun. However, significant deviations are known, which may be due to the influence of the overlying heliospheric magnetic field structure (Yurchyshyn, 2008 and references therein). The internal structure of MCs is helpful in understanding their solar origin. They also have important implications for their geoeffectiveness, as will be discussed in the next section.

4   CMEs and Geomagnetic Storms

Geomagnetic storms can be defined as disturbances of Earth's magnetosphere caused by the impact of IP magnetic field structures. The disturbance storm time (D_{st}) index, which is the average change in the horizontal component of Earth's magnetic field brought about by the geomagnetic storm as measured (in nT) at four low-latitude stations (see http://swdcwww.kugi.kyoto-u.ac.jp/dstdir/dst2/onDstindex.html for details), quantifies the intensity of the storms. In a typical magnetic storm, the D_{st} index suddenly increases from the zero level (the storm sudden commencement or SSC), drops to the zero level and then decreases to a minimum (negative) value before recovering back to the zero level. The minimum D_{st} value reached is considered as the intensity of the storm. Geomagnetic storms can be classified into five groups based on the minimum value of D_{st}: weak (-30 to -50 nT), moderate (-50 to -100 nT), strong (-100 to -200 nT), severe (-200 to -350 nT), and great (<-350 nT). It is also common to designate $D_{st} \leq -50$ nT as storm level (Loewe and Prolss, 1997). NOAA space weather scale uses the K_p index (planetary geomagnetic index) defined on a scale of 0 to 9 and the intensity levels are termed minor ($K_p = 5$), moderate ($K_p = 6$), strong ($K_p = 7$), severe ($K_p = 8$), and extreme ($K_p = 9$). Details can be found in http://www.swpc.noaa.gov/NOAAscales/. In our discussions we adopt a simpler scheme: $D_{st} \leq -50$ nT denotes storm level; -100 nT $< D_{st} \leq -50$ nT denotes moderate storms while $D_{st} \leq -100$ nT denotes intense storms. The relation between K_p and D_{st} is discussed in Vennerstroem (2001).

In order to get an idea on the frequency and intensity range of geomagnetic storms, we have shown the distribution of D_{st} values at or below -100 nT in Fig. 17. The number of such storms is typically ~100 in each solar cycle, based on the data available at the World Data Center in Kyoto (http://swdcwww.kugi.kyoto-u.ac.jp/
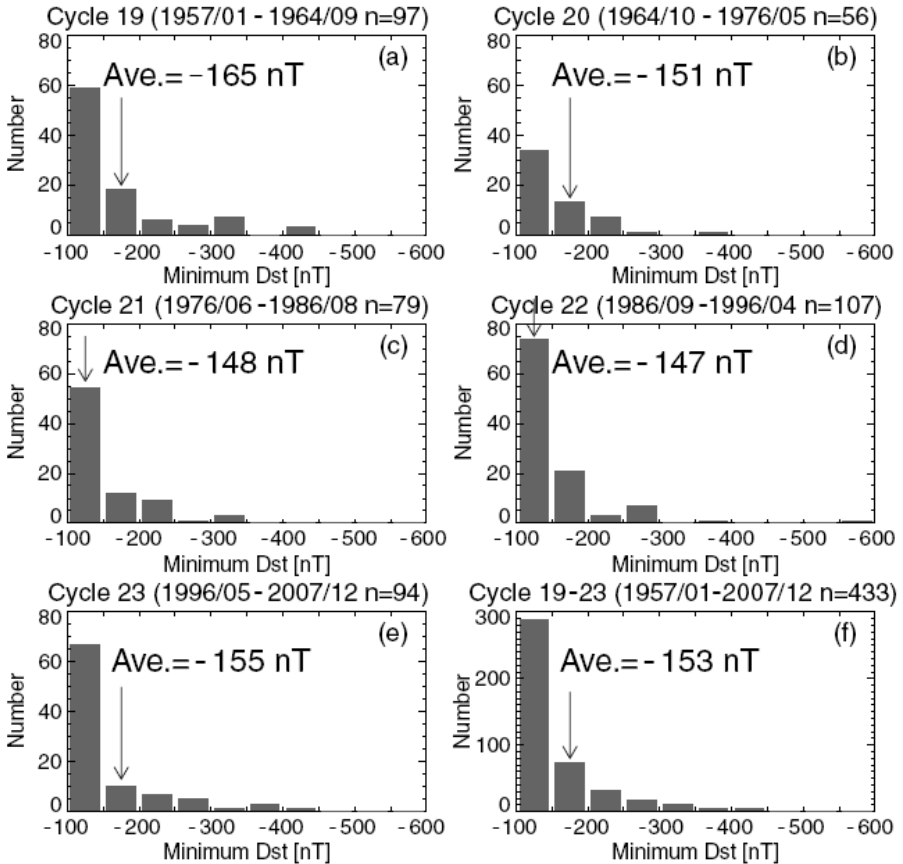
Fig. 17. D_{st} distribution for large geomagnetic storms ($D_{st} \leq -100$ nT) during the past five solar cycles (19–23). The duration and the number (n) of storms in cycle are given at the top of each plot.

dstdir/). Cycle 20 had the smallest number of storms (56), while cycle 22 had the largest (107). The combined set in Fig. 17(f) shows that the number of storms with $D_{st} \leq -300$ nT is rather rare. The strongest storms had $D_{st} < -600$ nT. It must be pointed out that not all the ≤ -100 nT storms are caused by ICMEs. It is known that ~ 10–15% of the large storms may be due to CIRs (Zhang *et al.*, 2007), but the D_{st} values are generally at the lower end (~ -100 nT), well below the average value of all the large storms.

The southward component of the IP magnetic field (B_s) reconnects with Earth's magnetic field in the dayside followed by another reconnection in the night-side enabling the coupling of the solar wind to the magnetosphere ultimately resulting in the buildup of the ring current. The D_{st} index essentially reflects the build up and decay of the ring current. The mechanism was first elucidated by Dungey (1961).

The CME connection to geomagnetic storms stems from the fact that CMEs are a source of B_s. While the heliospheric magnetic field under quiescent conditions does not have an out-of-the-ecliptic component ($B_z \sim 0$ except for some Alfvenic fluctuations), a CME introduces B_z by virtue of the flux rope structure and the sheath field that drapes the CME. The three distinct features of an ICME event, viz., the shock, the sheath, and the ejecta have corresponding signatures in D_{st} plots as SSC, the sheath storm and the ejecta (or cloud) storm (Tsurutani *et al.*, 1988). The ability of a CME or any IP structure to produce a geomagnetic storm is known as geoeffectiveness and such a structure is said to be geoeffective. Once a CME leaves the Sun, its ability to cause space weather effects depends on several factors: its arrival at Earth, its speed at Earth, and its magnetic field content (location and strength of B_s). These are discussed below in more detail.

4.1 CME arrival at Earth

CMEs have to reach Earth before causing geomagnetic storms. This happens when CMEs originate close to the disk center as discussed in Section 3.3 (see also Fig. 12). Occasionally, CMEs originating close to the disk center may not arrive at Earth because of deflection by nearby coronal holes (Gopalswamy *et al.*, 2008b) or faster CMEs merging with preceding slower ones. CMEs originating farther from the
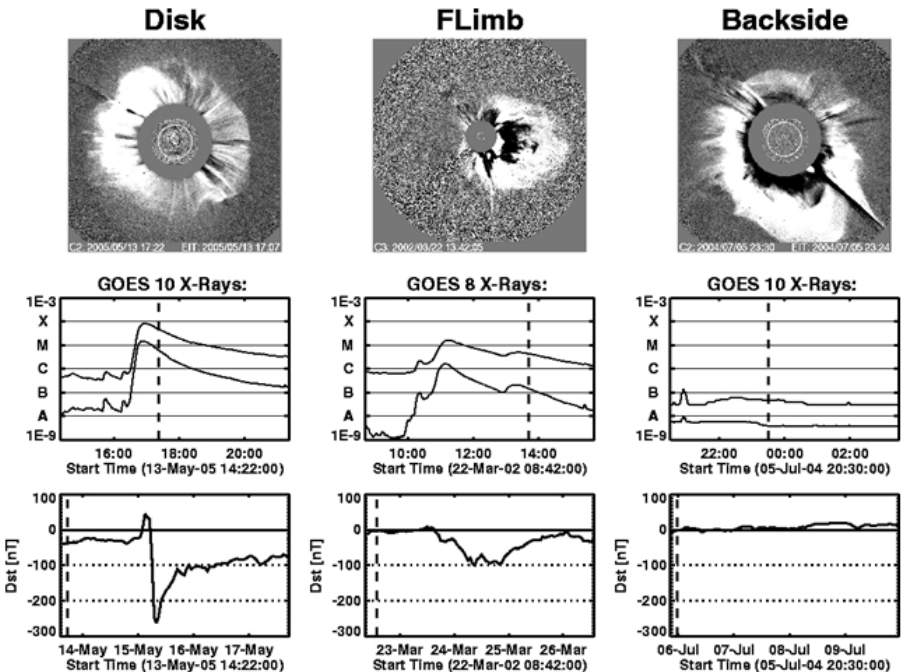

Fig. 18. Effect of solar source location on geoeffectiveness: (left) Halo CME from the disk center, (b) Halo CME originating from close to the limb but frontsided (FLimb), and (right) backside halo.

disk center also can cause geomagnetic storms, but what causes the storm is the B_s in the ICME sheath (Gosling *et al.*, 1990; Vennerstroem, 2001; Gopalswamy *et al.*, 2007; Gopalswamy *et al.*, 2008a and references therein). Since there is less chance for the sheath to have B_s than the whole ICME event, the geoeffectiveness of CMEs declines as a function of their solar source longitude (Gopalswamy *et al.*, 2007). This is illustrated in Fig. 18 using three halo CMEs originating from (i) close to the disk center, (ii) close to the limb but frontsided (Flimb), and (iii) backside of the Sun. The GOES soft X-ray light curve shows no changes for the backside CME because the flare is completely occulted. The disk-center halo results in a super storm ($D_{st} = -263$ nT), the Flimb halo results in a moderately intense storm ($D_{st} \sim -100$ nT), while the backside halo has no geomagnetic consequence at all ($D_{st} \sim 0$ nT). This result has also been confirmed statistically: $\sim$75% of disk halos and $\sim$60% of limb halos are geoeffective (Gopalswamy *et al.*, 2007) confirming the importance of the solar source location of CMEs. According to Fig. 12, we see that MC associated CMEs also originate close to the disk center, so the majority of MCs ($\sim$60%) are geoeffective.

One might wonder why all the disk halos and all the MCs are not geoeffective even though they originate close to the disk center. There are several possibilities: (i) CME cannibalism—fast halos catch up with slow ones, so only one ejecta arrives at Earth, (ii) CMEs are deflected away from the Sun-Earth line by coronal holes or by other CMEs, (iii) the ICMEs have no B_s (fully north pointing MCs) that they do not produce any geomagnetic storms, (iv) the magnitude of B_s is not high enough to cause a significant ($D_{st} \leq -50$ nT) storm. These exceptions need to be properly understood before assessing the geoeffectiveness of CMEs. It must be noted that cannibalism and coronal-hole deflection can also increase the geoeffectiveness of CMEs because interacting CMEs can enhance the southward component of the IP magnetic field, while coronal holes can deflect CMEs toward the Sun-Earth line.

4.2   Importance of CME speed

The geoeffectiveness also depends on the speed with which CMEs arrive at Earth. The D_{st} index is correlated with the ICME speed (provided the magnetic field has a B_s). Figure 19 shows that the D_{st} in the sheath and cloud portions correlate reasonably with the corresponding speeds ($r = 0.67$ for sheath D_{st} vs. sheath speed and $r = 0.65$ for MC D_{st} vs. MC speed). Interestingly, when we replace the sheath and MC speeds by the near-Sun speed of the associated CMEs, the correlation remains positive albeit weak ($r = 0.49$ for sheath D_{st} vs. CME speed and $r = 0.46$ for MC D_{st} vs. CME speed). The last set of correlations occurs because the near-Sun and near-Earth CME speeds are related via the IP acceleration discussed in Section 3.

4.3   Importance of CME magnetic field

Like the speed, the magnetic field content of the ICMEs also plays an important role. By this we mean the magnitude of B_s. The ICME magnetic field is also related to its speed: faster ICMEs tend to have higher magnetic field strength (Gonzalez *et al.*, 1998; Echer *et al.*, 2005; Gopalswamy *et al.*, 2008a). This is also true when the sheath and cloud portions of MCs are considered separately. Furthermore, faster CMEs near the Sun seem to result in MCs and sheaths with higher magnetic field
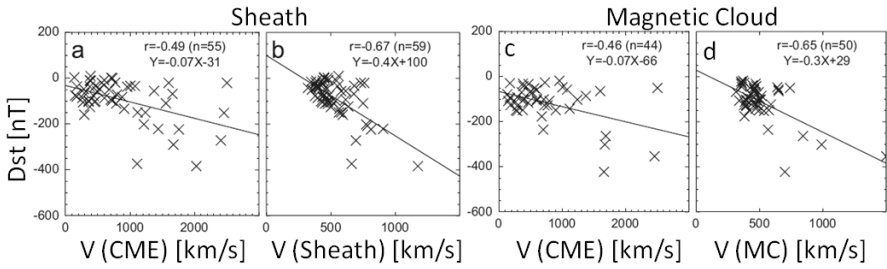
Fig. 19. D_{st} vs. speed plots for Sheaths and MCs. In (a) and (b), the D_{st} values correspond to the sheaths. In (c) and (d), the D_{st} values correspond to the cloud portion. The regression lines and the correlation coefficients (r) are shown on the plots.

Fig. 20. D_{st} vs. speed plots for Sheaths and MCs. In (a) and (b), the D_{st} values correspond to the sheaths. In (c) and (d), the D_{st} values correspond to the cloud portion. The regression lines and the correlation coefficients (r) are shown on the plots.
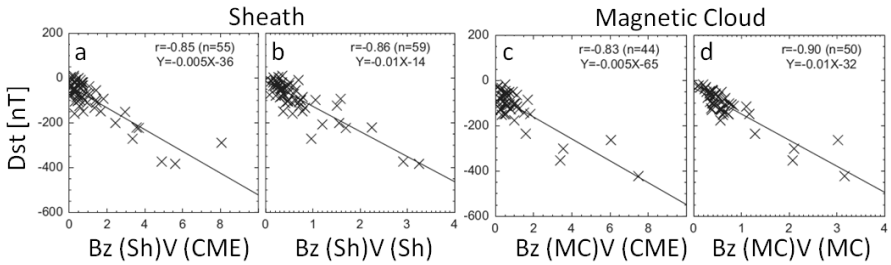
(Gopalswamy *et al.*, 2008a). The minimum D_{st} values are better correlated with the product of the field strength (or B_s) and speed in ICMEs, as shown in Fig. 20. Such a product is related to the well-known Epsilon function (Akasofu, 2002). Note that D_{st} has a high correlation with the speed-magnetic field (B_z) product in both the cloud and sheath portions with $r = 0.90$ and 0.86, respectively. As before, when we the replace the sheath and MC speeds by the near-Sun CME speed, the correlations remain very high: $r = 0.83$ and 0.85, respectively (see Fig. 20). This is an interesting result for space weather applications, especially because we do not have direct measurement of magnetic field inside CMEs near the Sun. If one can estimate the strength and orientation of the magnetic field in CMEs near the Sun, it will prove to be useful in predicting the occurrence of geomagnetic storms. It must be pointed out that we have considered only MCs and their sheaths in the above discussion. The result should be applicable to non-cloud ICMEs also.

4.4   Magnetic structure of MCs and geomagnetic storms

The four types of MCs discussed in Section 3.5 have important implications to the D_{st} profile of the resulting storms. Figure 21 shows the D_{st} profiles corresponding to
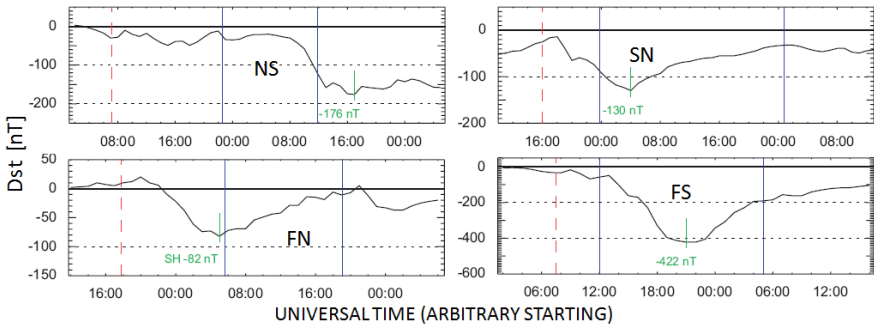
Fig. 21. Typical D_{st} profiles associated with the four types of MCs (NS: north-south, SN: south-north, FN: fully north, and FS: fully south) shown in Fig. 16. The cloud portions correspond to the interval between the vertical solid lines. The vertical dashed line indicates the shock. The D_{st} minimum values are notes on the plots, which represent the intensity of the geomagnetic storms associated with the MCs. For the NS MC, the storm peaks beyond the MC interval because the southward field is present only in the tail end of the MC. In the case of FN MC, the storm peak is before the MC interval because the southward field is present only in the sheath portion.

the four types of MCs described in Fig. 16. For NS MCs, the B_s occurs only in the trailing portion of the MC, so the storm occurs only during or after the tail portion. For SN MCs, the B_s occurs in the leading portion of the MC, so the storm peaks in the leading portion. For FS MCs, B_s is present throughout the MC, so the storm starts promptly upon arrival of the MC and the recovery starts only at the end of the MC interval (Gopalswamy *et al.*, 2005b). For FN MCs, there is no B_s during the MC interval, so they are not geoeffective at all (Yurchyshyn *et al.*, 2001). Thus one expects a large variability in the time at which the D_{st} minimum occurs with respect to the MC arrival at Earth. Additional time structure is caused by the presence of B_s in the sheaths preceding the MCs. If the sheath field has B_s and turns north before the MC interval, then one gets a double-dip storm (see e.g., Kamide *et al.*, 1998) for all MC types except for the FN MCs; in the case of FN MCs, all we get is a sheath storm.

Figure 22 shows the distribution of minimum D_{st} values in the cloud and sheath portions of MCs identified during solar cycle 23. The mean values of D_{st} in the cloud (-109 nT) and sheath (-90 nT) portions are at the intense storm level and comparable to each other. As noted above, the FN MCs are not geoeffective (average $D_{st} = -26$ nT, probably due to noise), while the FS MCs are most geoeffective (average $D_{st} = -125$ nT). The NS and SN MCs have similar average D_{st} values (-104 and -107 nT, respectively). The average D_{st} values in the sheath portions are at the storm level of all MC types with the FN MC sheaths being the most geoeffective (average $D_{st} = -132$ nT) and the FS MC sheaths the least geoeffective (average $D_{st} = -66$ nT). The NS and SN MC sheath storms are at the intermediate level: -75 nT and -85 nT, respectively.

The delay times of the D_{st} minima with respect to the arrival times of MCs are
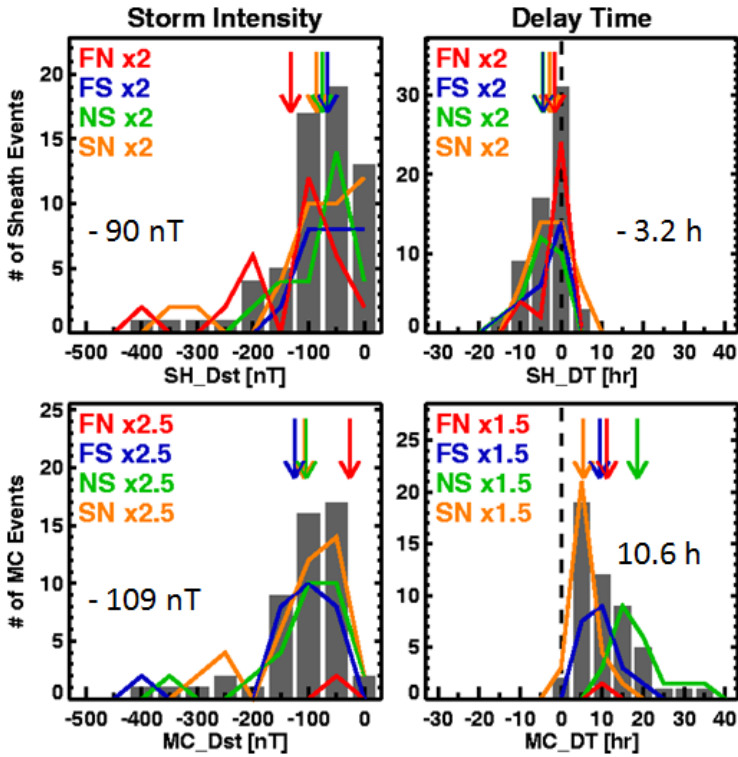
Fig. 22. Distributions of storm intensity (left) and delay time (right) for various MC types (colored lines) and all MCs (gray histogram). The values corresponding to the individual cloud types are multiplied by a suitable factor as indicated. The arrows point to the average values of the distributions. The average values corresponding to all events are also given on the plots. The vertical line on the delay time plots indicate the arrival time of MCs at the observing spacecraft.

also shown in Fig. 22. Sheaths arrive before the clouds, so the sheath storms peak before the MC arrival (average delay = −3.2 h). The cloud storms peak after MC arrival, as expected (average delay = +10.6 h). Among MC types, the delay time of cloud storms varies by a factor of ∼3, the smallest being for SN MCs (average delay ∼ +5.5 h) and the largest for NS MCs (average delay ∼ +18.6 h). The FS MCs have an intermediate delay (average delay ∼ +9.3 h). In a few cases, the sheath storms have their D_{st} minima after the MC arrival. This is because the sheath B_s occurs too close to the MC arrival and the D_{st} minimum typically occurs ∼2 h after $|B_s|$ attains its maximum value (Gonzalez and Echer, 2005). It must be noted that the magnetospheric tail current also contributes to the D_{st} minimum (Ohtani et al., 2001, 2005, 2007).

5   CMEs and Solar Energetic Particle Events

SEPs are so-called because their kinetic energy is much higher than that of the solar wind particles and they are of solar origin (in flares and CMEs) to distinguish them from cosmic rays, which are of galactic origin. SEP ions and electrons may suddenly have access to the inner magnetosphere during geomagnetic storms, where they can get trapped in a new radiation belt (Lorentzen *et al.*, 2002). During the largest SEP events, the energetic protons can penetrate all the way to Earth's atmosphere leading to significant ozone depletion (Jackman *et al.*, 2005). SEPs can damage the electronics of spacecraft, can pose radiation hazard to passengers and crew in high-flying aircraft, can harm humans in space, and may render satellites useless (see e.g., Turner, 2006) depending on the intensity of the SEPs. The SEP intensity is defined in terms of particle flux units (pfu, 1 pfu = 1 particle cm^{-2} s^{-1} sr^{-1}). SEPs of intensity exceeding 10 pfu in the >10 MeV energy channel are considered to be important for space weather. Occasionally the 10 MeV SEP intensity can exceed 10^4 pfu (see Gopalswamy *et al.*, 2005c).

5.1   Illustrative example

Figure 23 shows a large SEP event, plotted as the intensity of protons in three energy channels (>10 MeV, >50 MeV, and >100 MeV) as detected by the GOES satellite. Around the time of the sudden increase in SEP intensity (early on 2006 December 13), one can see a fast (1774 km/s) halo CME and a major solar flare (X-ray importance X3.4) in progress. The solar source of the flare was in the southwest quadrant (S06W23) on the Sun. The SEP intensity declines slowly in the three energy channels, until the ESP event that marks the arrival of the shock (which has been producing SEPs ever since it left the Sun). The shock arrival is also recorded by the ground based magnetometers and recognized as a positive excursion of the D_{st} index (SSC). The geomagnetic storm follows if the shock sheath or the driving ICME has a B_s component. The rapid decline of the SEP intensity after the shock arrival is due to the exclusion of the particles by the ICME analogous to the Forbush decrease.

5.2   Origin of SEPs: shock vs. flare

The connection between solar flares and SEPs was recognized early on (Forbush, 1946; Meyer *et al.*, 1956), and shocks of solar origin have also been thought to be another source of energetic particles (Uchida, 1960; Wild and Smerd, 1972). Kahler *et al.* (1978) established the link between CMEs and SEPs by identifying the CMEs as the drivers of the shocks that accelerate SEPs. Flares occur without CMEs, and produce energetic electrons (responsible for hard X-ray, microwave, and type III bursts) as well as protons. ESP events provide direct evidence for ion acceleration by shocks. Thus both flares and shocks can produce energetic particles. The current paradigm for SEPs is that impulsive, short-lived SEP events are due to flares and the large, gradual, long-lived events are accelerated in CME-driven shocks (see, e.g. Lin, 1987; Reames, 1999). Since all CMEs are associated with flares and higher-energy CMEs are associated with larger flares (see Fig. 8) one expects both flare and shock mechanisms operate simultaneously in every large eruptive event. However, since the spatial scale of flares is generally small (∼15° heliographic) one expects to observe both flare and shock components only during the well-connected events. Shocks are
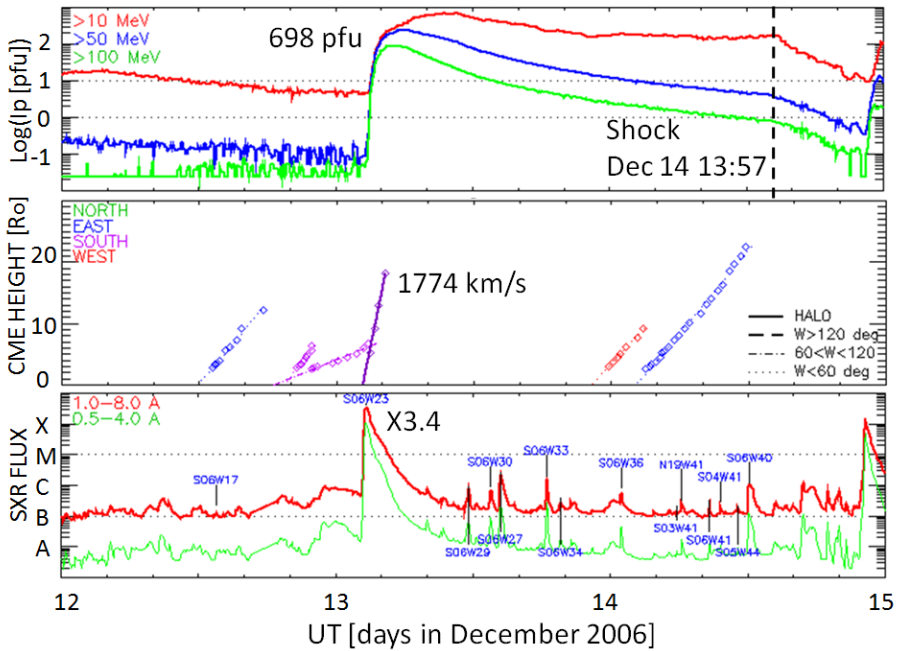
Fig. 23.   The gradual SEP event on 2006 Dec 13. (Top) Proton intensity in three energy channels (>10 MeV, >50 MeV, and >100 MeV). The proton intensity reached a maximum value of 698 particle flux units (pfu) in the >10 MeV energy channel (1 pfu = 1 particle per (cm^2.s.sr)). The SEP intensity dropped rapidly after the shock arrived at 1 AU on December 14 at 13:57 UT (marked by the vertical dashed line). (Middle) Height-time plots of all CMEs that occurred over a three-day period. The fast (1774 km/s) halo CME on December 13 at 02:54 was responsible for the SEP event in question. (Bottom) GOES soft X-ray light curves in two energy channels (1.0–8.0 Å and 0.5–4.0 Å). Several flares occurred during the three-day period most of them coming from the active region NOAA 0930. The X3.4 flare associated with the SEP event occurred on December 13 at 02:40 UT.

more extended so the solar source can occur in wide range of longitudes, still favoring the western location because of the Parker-spiral structure of the interplanetary magnetic field that carries the particles to a detector near Earth. Figure 24(a) shows the solar sources of shock-producing CMEs inferred from DH type II radio bursts, with the SEP-producing subset distinguished. The shock-driving CMEs need to originate from the central meridian to western longitudes to produce an SEP event detectable at Earth. Figure 24(b) shows that the SEP association rate of radio-emitting CMEs peaks in the western hemisphere at ∼69° longitude with a broad longitudinal distribution. Note that more than half of the CMEs originating from behind the west limb can result in SEP events, which is possible only when the shocks accelerate the particles. SEP events that result in high energy particles penetrating Earth's atmosphere are known as ground level enhancement (GLE) events (Cliver, 2006; Lopate, 2006). The solar sources of the GLE events are generally well-connected and hence a flare
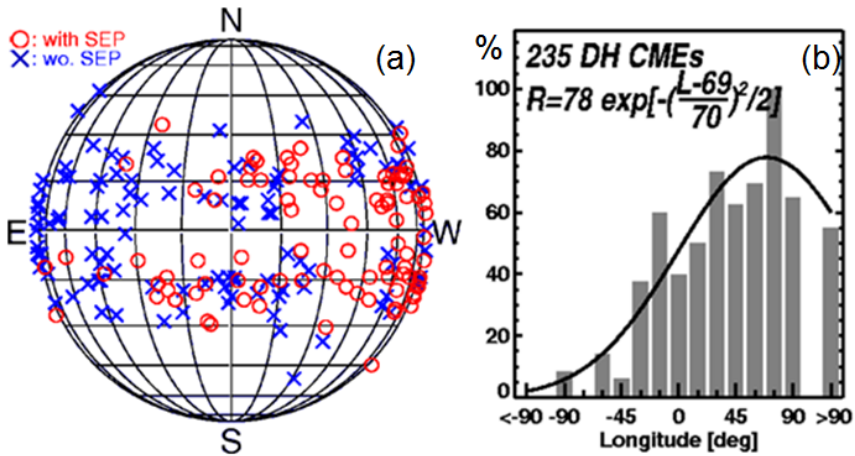
Fig. 24.   (Left) Heliographic coordinates of CMEs that produce type II radio bursts in the decame-ter-hectometric wavelengths (all symbols). The subset associated with SEP events (with intensities ≥ 1 pfu) are denoted by the open circles. (Right) The SEP association rate (R) of CMEs that produce DH type II bursts, plotted as a function of CME source longitude (L). The curve fitted to the distribution is given on the plot. The distribution peaks at $L = 69°$ and has a width of $70°$. Note that there are no SEP events associated with CMEs from behind the east limb, but many from CMEs originating from behind the west limb.

origin is often assumed. However, several GLE events with poor connectivity have been reported in the literature (Cliver, 1981, 2006; Kudela *et al.*, 1993). In cycle 23, a single GLE event (2001 April 18) originated from $\sim 30°$ behind the west limb, yet the GLE event was well observed and ranked the fifth largest in cycle 23 (Gopalswamy, 2008a). It is highly unlikely that the flare component was observed in this GLE event.

Extensive comparison between SEPs and CMEs became possible only during cy-cle 23, which led to the result that large SEP events are invariably associated with fast and wide CMEs (Fig. 25). The average sky-plane speed of SEP-associated CMEs is ~ 1623 km/s, much larger than the average speed of all CMEs (see Fig. 3). Most of the SEP-associated CMEs are also halo or partial halo CMEs confirming their higher energy. The speeds of GLE-associated CMEs are the highest, suggesting that they constitute the high-energy subset of the SEP-associated CMEs. Among the 16 GLE events detected in cycle 23, only two CMEs had speed less than 1500 km/s (938 km/s on May 02 and 1099 km/s on May 06 in 1998). Two such CMEs have also been reported for cycle 21 GLEs. Cliver (2006) noted that the two eruptions occurred when SEP background was elevated, which might imply an efficient shock acceleration as suggested by Gopalswamy *et al.* (2004). Another factor to be con-sidered is the Alfven speed distribution in the corona (Gopalswamy *et al.*, 2001c; Mann *et al.*, 2003), which can vary anywhere from a few hundred km/s to more than 1600 km/s (Gopalswamy *et al.*, 2008c, d) in the outer corona where the GLEs and SEPs are released. Therefore, one cannot rule out the possibility that the lower speed
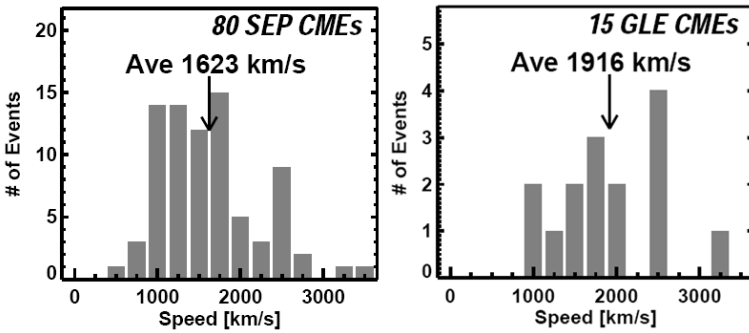
Fig. 25.   Speed distributions for CMEs associated with SEP events (left) and GLE events (right) from solar
cycle 23.   The average values of the distributions are noted on the plots.   There were actually 16 GLE
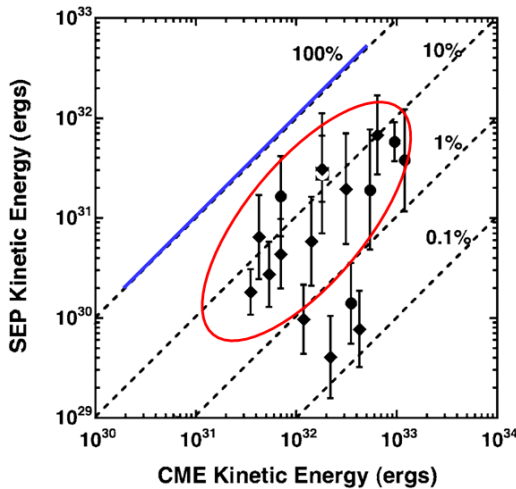events in cycle 23, but one did not have CME observations.

Fig. 26.   Scatter plot between the CME kinetic energy and the SEP kinetic energy for a set of events
during solar cycle 23.   The blue line is the bisector.   The dashed lines represent the fraction of CME
kinetic energy (100%, 10%, 1%, and 0.1%) that goes into SEP kinetic energy.   The red ellipse encircles
the events that lie near the 10% level.   (With kind permission from Springer Science+Business Media:
Space Sci. Rev., Solar energetic particle composition, energy spectra, and space weather, **124**, 2006,
303–316, Mewaldt, R. A., figure 5.)

CMEs associated with GLEs propagate into a medium with low Alfven speed.   This
also applies to some SEP events with low-speed CMEs (Gopalswamy *et al.*, 2008d).
Another observational evidence for the close connection between CMEs and SEPs is
the fraction of CME kinetic energy that goes into SEPs: For a set of 16 well observed

SEP events, the SEP kinetic energy constitutes ~10% CME kinetic energy (Fig. 26), which represents a high efficiency of particle acceleration by shocks (Mewaldt, 2006). Since the typical kinetic energy of SEP-producing CMEs is $>10^{32}$ erg, we see that large SEP events have an energy content of at least 10^{31} erg.

5.3   SEP release sites from shocks and flares

The presence of a type II burst in all SEP events implies the presence of a shock early in the event (Gopalswamy *et al*., 2002; Cliver *et al*., 2004). When the type II burst starts in the corona, the CME leading edge is typically in the heliocentric distance range of 1.7–2.0R_o, which means the CME-driven shock is also located at similar heights (Gopalswamy *et al*., 2005a). On the other hand, the SEP release seems to happen when the CME is farther out in the corona, in the range 4–8R_o (Kahler, 1994; Gopalswamy *et al*., 2005d; Gopalswamy, 2008b). However, flare energy release takes place in the inner corona, typically at a heliocentric distance of ~1.03R_o. Since the shock is more extended than the CME located radially above the flare site, the flare particles (if at all they escape) have to pass through the shock front and may be further accelerated. Under the standard CSHKP eruption scenario, the CME flux rope forms due to reconnection, so particles accelerated in the reconnection region flow downwards to produce gamma ray lines and pion continuum (when the particle energy is very high—hundreds of MeV). As we noted before, the particles precipitate over a narrow range of angles, and may be injected over the same range in the direction away from the Sun (Cliver and Ling, 2007). It appears that the SEPs will be trapped in the CME flux rope and may not freely propagate into the IP medium, unless the accelerated ions have access to open field lines. Evidence for high energy (100s of keV to MeV) electrons trapped in moving CME structures is known for a long time from moving type IV radio bursts (see e.g. Gopalswamy and Kundu, 1989; Bastian *et al*., 2001), and moving hard X-rays sources (Hudson *et al*., 2001). But ions do not produce electromagnetic signatures, so we do not know if they are trapped in the flux rope. On the other hand, every large SEP event is associated with a type III bursts in the beginning (Cane *et al*., 2002; Gopalswamy *et al*., 2005d), which means energetic electrons from the reconnection site do escape from the flare site along open field lines (unless these electrons are also from the shock). There is no reason why the ions should not propagate along these field lines, thus indicating the possibility of a flare component to the large SEP events.

5.4   Challenges to shock acceleration paradigm

Despite the close correspondence between CMEs and SEP events, there are some discrepancies. For example, the CME speed and SEP intensity are reasonably corre-lated, yet the scatter is very large (Kahler, 2001; Gopalswamy *et al*., 2003d). CME-driven shocks take in what lies ahead of them to accelerate and inject back into the heliosphere. This so-called source material is not just the ordinary solar wind, but can be ions from impulsive solar flares and previous gradual events, CIR events, pickup ions, CME ejecta, and the suprathermal tail of the solar wind (Gopalswamy *et al*., 2004; Tylka *et al*., 2005; Mewaldt, 2006). In fact, CMEs associated with most of the large SEP events seem to be propagating through a medium disturbed and dis-torted by preceding CMEs, a process described as preconditioning (Gopalswamy *et*
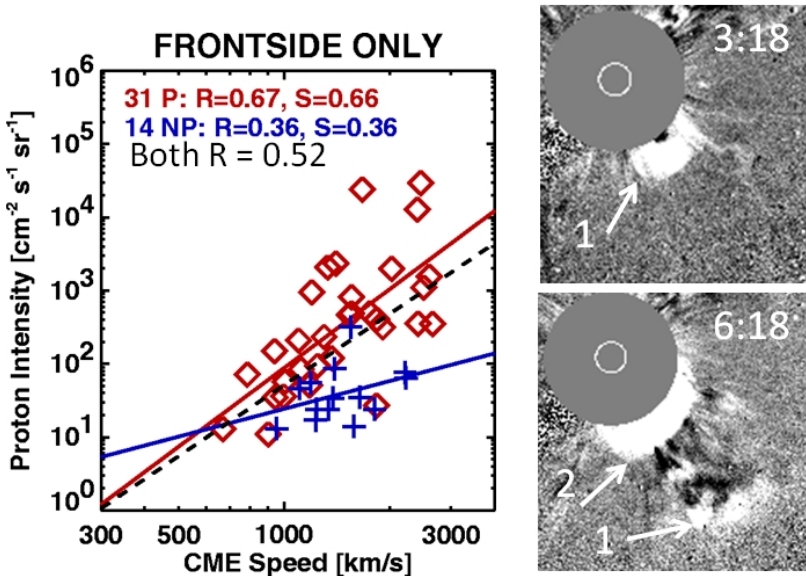
Fig. 27. (Left) Scatter plot between SEP intensity and CME speed. CMEs with (P) and without (NP) preceding CMEs are distinguished by different symbols. The correlation coefficients are shown for the two populations and for the combined set ($R = 0.52$). (Right) CMEs corresponding to one of the events used in the scatter plot, which occurred on 2001 October 1. The first CME (marked 1) appeared at 03:18 UT from an active region close to the southwest limb. While CME 1 was in progress the second one (marked) appeared at 06:18 UT from the same active region. Note that CME 2 propagates into the preceding CME and the associated disturbance rather than through the normal interplanetary medium.

al., 2003d, 2004). In order to investigate how the preceding CMEs affect the SEP intensity, Fig. 27 shows a scatter plot between CME speed and the SEP intensity; events with preceding CMEs (P) and no preceding CMEs (NP) are distinguished. The combined set of all SEP events has a correlation coefficient (r) of only 0.52. On the other hand, the P events have a much better correlation ($r = 0.67$) and the NP events have a poorer correlation ($r = 0.36$). In addition, P events consistently have a higher intensity than the NP events, so that the P and NP population occupy distinct regions in the scatter plot, thus explaining the large scatter in the CME speed vs. SEP intensity plot. Figure 27 also shows the CMEs involved in one of the SEP events used in the scatter plot: CME 2 is ejected directly behind a preceding CME (marked 1) that left from the same active region a few hours earlier. In the 06:18 UT SOHO/LASCO frame, one can see that what lies ahead of the SEP producing CME is the preceding CME, not the ordinary solar wind as in the 03:18 UT frame. Kahler and Vourlidas (2005) confirmed the above result, but attributed the difference between high and low intensity SEP events to the high and low brightness, respectively of the associated CMEs. Low brightness can also result if a CME propagates through a tenuous medium so it cannot sweep up more material.
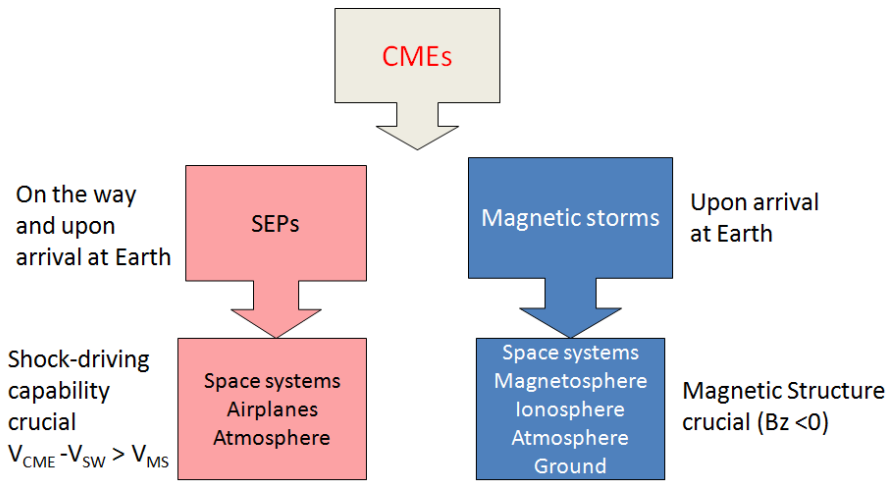
Fig. 28. The two primary interplanetary consequences of CMEs: SEPs and magnetic storms. SEPs are produced by CME-driven shocks on the way and upon arrival at Earth. CME speed (V_{CME}) in excess of the solar wind speed (V_{SW}) must exceed the magnetosonic speed (V_{MS}) to drive shocks. The SEPs affect space systems (with or without humans), passengers in high-altitude airplanes, and Earth's atmosphere. Geomagnetic storms are produced only when CMEs arrive at Earth with the additional condition that they possess south-pointing magnetic fields ($B_z < 0$). Geomagnetic storms have consequences to space systems, the entire geospace and even to the ground.

6 Summary

The two key space weather aspects of CMEs (SEPs and geomagnetic storms) and their geospace consequences are summarized in Fig. 28. CMEs responsible for SEPs and magnetic storms have different paths in the heliosphere, with some overlap. The spatial domains where the space weather effects are generated are also different. SEP production typically starts when the CME-driven shock is within a few solar radii from the Sun. The shock continues to produce SEPs in the IP medium so long as it is strong enough. When the shock arrives at the observing spacecraft, a sudden increase in SEP intensity is observed (the ESP event). Production of geomagnetic storms, on the other hand, happens only upon the arrival of B_s in the CME and/or the sheath at Earth's magnetosphere.

The shock-driving ability of a CME is crucial for the production of SEPs and the shocks need to be strong enough to efficiently accelerate SEPs. The coronal and interplanetary environment also plays a role in determining the strength of the shocks because the Alfven speed can vary by a factor of 4 in this region. The shock is also important for geoeffective CMEs in compressing the magnetosphere, but the intensity and duration of the southward component of the magnetic field in the shock sheath and ICME determine the strength of the resulting magnetic storm. Thus the magnetic structure of the ICME is important for geomagnetic storms, but not for SEPs.

Table 1 shows a compilation of the numbers of solar and interplanetary events
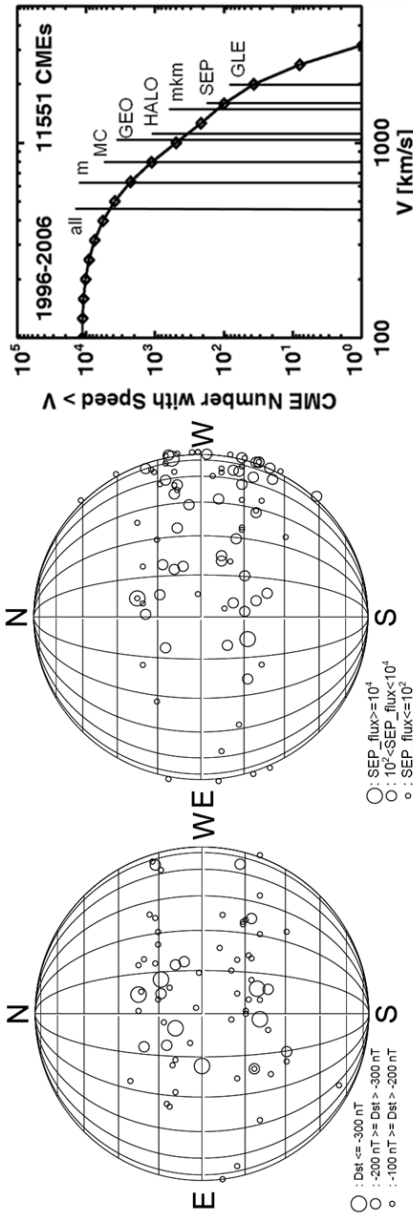
Fig. 29. Comparing the source location and speed of CMEs producing SEPs and geomagnetic storms. (Left) Source locations of geoeffective CMEs with large, medium and small circles representing storms with $D_{st} \leq -300$ nT, -200 nT $\geq D_{st} > -300$ nT, and -100 nT $\geq D_{st} > -200$ nT, respectively. (Middle) Source locations of SEP-associated CMEs with large, medium and small circles representing SEP events with peak flux $\geq 10^4$ pfu, in the range 10^2 to 10^4 pfu, and $\leq 10^2$ pfu, respectively. (Right) Cumulative distribution of CMEs, with the average speeds of various subsets: m (metric type II bursts), MC (magnetic clouds), GEO (geomagnetic storms), HALO (halo CMEs), mkm (type II bursts extending from metric to kilometric wavelengths), SEP (solar energetic particles), and GLE (ground level enhancement). The average speed of all CMEs is also shown for comparison (all).

Table 1. List of solar and interplanetary events important for space weather.

Event type	Rise	Max	Decl	Total	V_{CME} (km/s)
All CMEs ($W > 30°$)	962	3516	3261	7739	450[a]
Magnetic clouds	20	29	20	69	774[b]
Non-cloud ICMEs	17	72	35	124	960[c]
Frontside Halos	30	116	91	237	1052[b]
Major storms	12	32	25	69	1042[b]
Shocks (in situ)	34	110	72	226	987[d]
IP Type II bursts	28	125	104	257	1532[e]
Large SEP events	5	38	33	76	1623[f]

[a]For CMEs in Fig. 4; [b]from Gopalswamy *et al*. (2008a); [c]events in Fig. 14; [d]from Gopalswamy *et al*. (2009) (under preparation); [e]from Gopalswamy *et al*. (2008d); [f]from Fig. 25.

relevant for space weather. For each event type, the average sky-plane speed of the associated LASCO CMEs is given in the last column. Clearly only a tiny fraction of all CMEs (∼3% or less) are important for space weather. The numbers are also binned into the three phases of the solar cycle 23. There is a general solar-cycle dependence of the numbers, the most coming from the maximum phase. The numbers of in situ shocks, IP type II bursts, and halo CMEs are similar (and much higher than the others); these phenomena happen when the associated CMEs meet special conditions in terms of source location on the Sun and magnetic connectivity to Earth. The last column shows that the speeds of the associated CMEs range from ∼770 km/s to 1600 km/s, suggesting that these CMEs are very energetic. The CMEs causing major geomagnetic storms (geoeffective CMEs) have an average speed of ∼1000 km/s, intermediate between those of halo CMEs and MC-associated CMEs. On the other hand, the speed of SEP associated CMEs is about 50% higher. This may not be a major difference if we take into account of the projection effects. Only a subset of SEP associated CMEs are close to the disk center, while most of the geoeffective CMEs originate there. Therefore, the geoeffective CMEs are subject to projection effects and their true speed is likely to be higher. Thus, we can conclude that both SEP producing and geoeffective CMEs are very energetic.

Figure 29 summarizes the source and kinematic properties of CMEs that produce SEPs and geomagnetic storms in comparison with other energetic CME populations. Storm-producing CMEs originate close to the disk center of the Sun, while the SEP-associated CMEs are mostly confined to the western hemisphere. Exceptions are the smaller events in both categories. The source locations of the two populations are distinct because the CME and SEP arrival at Earth take different paths: SEPs follow the magnetic field lines, while CMEs propagate radially away from the Sun. The cumulative number of CMEs in Fig. 29 drops precipitously at speeds >3000 km/s. In fact, there were only 9 CMEs with speed >2500 km/s among the 13000 + CMEs detected until the end of 2007. There were only two CMEs with speed exceeding 3000 km/s. This tells us that there is a limit to the CME kinetic energy. This limit

can be traced to the amount of free energy that can be stored in the source active region. Since the amount of free energy is of the order of potential energy of the source magnetic fields, this translates into the maximum field strength in large active regions, known to be within ~5000 G. An important consequence of the speed limit is that the associated shocks take a finite time to reach Earth. Historical data on fast-transit shocks (Cliver *et al.*, 1990) and empirical modeling (Gopalswamy *et al.*, 2005c) suggest such a limit to the shock travel time, thus allowing a warning of at least about half a day.

References

Aguilar-Rodriguez, E., X. Blanco-Cano, and N. Gopalswamy, Composition and magnetic structure of interplanetary coronal mass ejections at 1 AU, *Adv. Space Res.*, **36**, 522, 2006.

Akasofu, S.-I., Predicting geomagnetic storms as a space weather project, in *Space Weather Study using Multi-point Techniques*, edited by L.-H. Lyu, p. 3, COSPAR Colloquia series 12, 2002.

Bastian, T. S., M. Pick, A. Kerdraon, D. Maia, and A. Vourlidas, The coronal mass ejection of 1998 April 20: Direct imaging at radio wavelengths, *Astrophys. J.*, **558**, L65, 2001.

Biesecker, D. A. *et al.*, Solar phenomena associated with "EIT waves", *Astrophys. J.*, **569**, 1009, 2002.

Bothmer, V. and R. Schwenn, Eruptive prominences as sources of magnetic clouds in the solar wind, *Space Sci. Rev.*, **70**, 215, 1994.

Burlaga, L., E. Sittler, F. Mariani, and R. Schwenn, Magnetic loop behind an interplanetary shock—Voyager, Helios, and IMP 8 observations, *J. Geophys. Res.*, **86**, 6673, 1981.

Burkepile, J. T., A. J. Hundhausen, A. L. Stanger *et al.*, Role of projection effects on solar coronal mass ejection properties: 1. A study of CMEs associated with limb activity, *J. Geophys. Res.*, **109**, A03103, 2004.

Cane, H. V. and I. Richardson, Interplanetary coronal mass ejections in the near-Earth solar wind during 1996-2002, *J. Geophys. Res.*, **108**, SSH 6-1, 2003.

Cane, H. V., W. C. Erickson, and N. P. Prestage, Solar flares, type III radio bursts, coronal mass ejections, and energetic particles, *J. Geophys. Res.*, **107**, 1315, 2002.

Carrington, R. C., Description of a singular appearance seen in the Sun on September 1, 1859, *MNRAS*, **20**, 13, 1860.

Chen, J., R. A. Howard, G. E. Brueckner *et al.*, Evidence of an erupting magnetic flux rope: LASCO coronal mass ejection of 1997 April 13, *Astrophys. J.*, **490**, L191, 1997.

Chen, P. F., The relation between EIT waves and solar flares, *Astrophys. J.*, **641**, L153, 2006.

Cliver, E. W., Prompt injection of relativistic protons from the September 1, 1971 solar flare, *Sol. Phys.*, **75**, 341, 1981.

Cliver, E. W., The unusual relativistic solar proton events of 1979 August 21 and 1981 May 10, *Astrophys. J.*, **639**, 1206, 2006.

Cliver, E. W. and A. G. Ling, Electrons and protons in solar energetic particle events, *Astrophys. J.*, **658**, 1349, 2007.

Cliver, E. W., J. Feynman, and H. B. Garrett, An estimate of the maximum speed of the solar wind, 1938-1989, *J. Geophys. Res.*, **95**, 17103, 1990.

Cliver, E. W., D. F. Webb, and R. A. Howard, On the origin of solar metric type II bursts, *Sol. Phys.*, **187**, 89, 1999.

Cliver, E. W., S. W. Kahler, and D. V. Reames, Coronal shocks and solar energetic proton events, *Astrophys. J.*, **605**, 902, 2004.

Cliver, E. W., M. Laurenza, M. Storini, and B. J. Thompson, On the origins of solar EIT waves, *Astrophys. J.*, **631**, 604, 2005.

Cohen, C. M. S., Observations of energetic storm particles: An overview, *AGU Monograph 165*, 275, 2006.

Dal Lago, A., R. Schwenn, and W. D. Gonzalez, Relation between the radial speed and theexpansion speed of coronal mass ejections, *Adv. Space Res.*, **32**, 2637, 2003.

Dulk, G. and D. J. McLean, Coronal magnetic fields, *Sol. Phys.*, **57**, 279, 1978.

Dungey, J. W., Interplanetary magnetic field and the auroral zones, *Phys. Rev. Lett.*, **6**, 47, 1961.

Echer, E., M. V. Alves, and W. D. Gonzalez, A statistical study of magnetic cloud parameters and geoeffectiveness, *J. Atmos. Sol.-Terr. Phys.*, **67**, 839, 2005.

Elliott, H. A., D. J. McComas, N. A. Schwadron *et al.*, An improved expected temperature formula for identifying interplanetary coronal mass ejections, *J. Geophys. Res.*, **110**, A04103, 2005.

Feynman, J. and S. F. Martin, The initiation of coronal mass ejections by newly emerging magnetic flux, *J. Geophys. Res.*, **100**, 3355, 1995.

Filippov, B. P., Causes and effects of filament eruptions (review), in *New Perspectives on Solar Prominences (IAU Colloquium 167)*, edited by D. Rust, D. F. Webb, and B. Schmieder, Vol. 150, p. 342, 1998.

Forbush, S., Three unusual cosmic-ray increases possibly due to charged particles from the Sun, *Phys. Rev.*, **70**, 771, 1946.

Gold, T., Magnetic storms, *Space Sci. Rev.*, **1**, 100, 1962.

Gonzalez, W. D., A. L. Clua de Gonzalez, A. Dal Lago *et al.*, Magnetic cloud field intensities and solar wind velocities, *Geophys. Res. Lett.*, **25**(7), 963, 1998.

Gonzalez, W. D. and E. Echer, A study on the peak Dst and peak negative Bz relationship during intense geomagnetic storms, *Geophys. Res. Lett.*, **32**, L18103, 2005.

Gopalswamy, N., X-ray and microwave signatures of coronal mass ejections, in *Solar Physics with Radio Observations*, edited by T. Bastian, N. Gopalswamy, and K. Shibasaki, NRO Report No. 479, p. 141, 1999.

Gopalswamy, N., Relation between coronal mass ejections and their interplantary counterparts, *COSPAR Colloquia Series 14*, 157, 2002.

Gopalswamy, N., A global picture of CMEs in the inner heliosphere, in *The Sun and the Heliosphere as an Integrated System*, edited by G. Poletto and S. T. Suess, p. 201, Kluwer, Boston, 2004.

Gopalswamy, N., Coronal mass ejections of solar cycle 23, *J. Astrophys. Astron.*, **27**, 243, 2006a.

Gopalswamy, N., Consequences of coronal mass ejections in the heliosphere, *Sun and Geosphere*, **1**(2), 5, 2006b.

Gopalswamy, N., Properties of interplanetary coronal mass ejections, *Space Sci. Rev.*, **124**, 145, 2006c.

Gopalswamy, N., Coronal mass ejections and type II radio bursts, *AGU Monograph 165*, 207, 2006d.

Gopalswamy, N., Solar connections of geoeffective magnetic structures, *J. Atmos. Sol.-Terr. Phys.*, **70**, 2078, doi:10.1016/j.jastp.2008.06.010, 2008a.

Gopalswamy, N., Type II radio emission and solar energetic particle events, *AIP Conference Proceedings*, **1039**, p. 196, 2008b.

Gopalswamy, N. and M. R. Kundu, Radioheliograph and white-light coronagraph studies of a coronal mass ejection event, *Sol. Phys.*, **122**, 145, 1989.

Gopalswamy, N., Y. Hanaoka, T. Kosugi *et al.*, On the relationship between coronal mass ejections and magnetic clouds, *Geophys. Res. Lett.*, **25**, 2485, 1998.

Gopalswamy, N., A. Lara, R. P. Lepping, M. L. Kaiser, D. Berdichevsky, and O. C. St. Cyr, Interplanetary acceleration of coronal mass ejections, *Geophys. Res. Lett.*, **27**, 145, 2000.

Gopalswamy, N., S. Yashiro, M. L. Kaiser, R. A. Howard, and J.-L. Bougeret, Characteristics of coronal mass ejections associated with long-wavelength type II radio bursts, *J. Geophys. Res.*, **106**, 29219, 2001a.

Gopalswamy, N., A. Lara, S. Yashiro, M. L. Kaiser, and R. A. Howard, Predicting the 1-AU arrival times of coronal mass ejections, *J. Geophys. Res.*, **106**, 29207, 2001b.

Gopalswamy, N., A. Lara, M. L. Kaiser, and J.-L. Bougeret, Near-Sun and near-Earth manifestations of solar eruptions, *J. Geophys. Res.*, **106**, 25,261-25,278, 2001c.

Gopalswamy, N., S. Yashiro, G. Michalek *et al.*, Interacting coronal mass ejections and solar energetic particles, *Astrophys. J.*, **572**, L103, 2002.

Gopalswamy, N., A. Lara, S. Yashiro, S. Nunes, and R. A. Howard, Coronal mass ejection activity during solar cycle 23, *ESA SP-535*, 403, 2003a.

Gopalswamy, N., A. Lara, S. Yashiro, and R. A. Howard, Coronal mass ejections and solar polarity reversal, *Astrophys. J.*, **598**, L63, 2003b.

Gopalswamy, N., M. Shimojo, W. Lu, S. Yashiro, K. Shibasaki, and R. A. Howard, Prominence eruptions and coronal mass ejection: A statistical study using microwave observations, *Astrophys. J.*, **586**, 562, 2003c.

Gopalswamy, N., S. Yashiro, A. Lara *et al.*, Large solar energetic particle events of cycle 23: A global view, *Geophys. Res. Lett.*, **30**(12), SEP 3-1, 2003d.

Gopalswamy, N., S. Yashiro, S. Krucker, G. Stenborg, and R. A. Howard, Intensity variation of large solar energetic particle events associated with coronal mass ejections, *J. Geophys. Res.*, **109**, A12105, 2004.

Gopalswamy, N., E. Aguilar-Rodriguez, S. Yashiro *et al.*, Type II radio bursts and energetic solar eruptions, *J. Geophys. Res.*, **110**, A12S07, 2005a.

Gopalswamy, N., S. Yashiro, G. Michalek, H. Xie, R. P. Lepping, and R. A. Howard, Solar source of the largest geomagnetic storm of cycle 23, *Geophys. Res. Lett.*, **32**, L12S09, 2005b.

Gopalswamy, N., S. Yashiro, Y. Liu *et al.*, Coronal mass ejections and other extreme characteristics of the 2003 October-November solar eruptions, *J. Geophys. Res.*, **110**, A09S15, 2005c.

Gopalswamy, N., H. Xie, S. Yashiro, and I. Usoskin, Coronal mass ejections and ground level enhancements, *Proc. 29th International Cosmic Ray Conference*, Pune, p. 169, 2005d.

Gopalswamy, N., A. Lara, P. K. Manoharan, and R. A. Howard, An empirical model to predict the 1-AU arrival of interplanetary shocks, *Adv. Space Res.*, **36**(12), 2289, 2005e.

Gopalswamy, N., S. Yashiro, and S. Akiyama, Coronal mass ejections and space weather due to extreme events, in *Proceedings of the ILWS Workshop*, edited by N. Gopalswamy and A. Bhattacharyya, Quest, Mumbai, p.79, 2006.

Gopalswamy, N., S. Yashiro, and S. Akiyama, Geoeffectiveness of halo coronal mass ejections, *J. Geophys. Res.*, **112**, A06112, 2007.

Gopalswamy, N., S. Akiyama, S. Yashiro, G. Michalek, and R. P. Lepping, Solar sources and geospace consequences of interplanetary magnetic clouds observed during solar cycle 23, *J. Atmos. Sol.-Terr. Phys.*, **70**, 245, 2008a.

Gopalswamy, N., P. Mäkelä, H. Xie, S. Akiyama, and S. Yashiro, CME interaction with coronal holes and their interplanetary consequences, *J. Geophys. Res.*, doi:10.1029/2008JA013686, 2008b (in press).

Gopalswamy, N., S. Yashiro, H. Xie *et al.*, Radio-quiet fast and wide coronal mass ejections, *Astrophys. J.*, **674**, 560, 2008c.

Gopalswamy, N., S. Yashiro, S. Akiyama, P. Mäkelä, H. Xie, M. L. Kaiser, R. A. Howard, and J.-L. Bougeret, Coronal mass ejections, type II radio bursts, and solar energetic particle events in the SOHO era, *Ann. Geophys.*, **26**, 1, 2008d.

Gopalswamy, N., A. Dal Lago, S. Yashiro, and S. Akiyama, The expansion and radial speeds of coronal mass ejections, *Cent. Eur. Astrophys. Bull. 1*, 2008e (in press).

Gosling, J. T., Coronal mass ejections and magnetic flux ropes in interplanetary space, in *Physics of Magnetic Flux Ropes, AGU Monograph 58*, p. 343, 1990.

Gosling, J. T., The solar flare myth, *J. Geophys. Res.*, **98**, 18937, 1993.

Gosling, J. T., D. J. McComas, J. L. Phillips, and S. J. Bame, Coronal mass ejections and large geomagnetic storms, *Geophys. Res. Lett.*, **17**, 901, 1990.

Hanaoka, Y., H. Kurokawa, S. Enome *et al.*, Simultaneous observations of a prominence eruption followed by a coronal arcade formation in radio, soft X-rays, and H-alpha, *PASJ*, **46**, 205, 1994.

Harrison, R. A., Bursting the solar bubble: the flare - coronal mass ejection relationship, in *Solar Eruptions and Energetic Particles, AGU Monograph Series 165*, 73, 2006.

Harrison, R. A., C. J. Davis, C. J. Eyles *et al*., First imaging of coronal mass ejections in the heliosphere viewed from outside the Sun Earth line, *Sol. Phys.*, **247**, 171, 2008.

Henke, T., J. Woch, R. Schwenn *et al*., Ionization state and magnetic topology of coronal mass ejections, *J. Geophys. Res.*, **106**, 10,597, 2001.

House, L. L., W. J. Wagner, E. Hildner, C. Sawyer, and H. U. Schmidt, Studies of the corona with the Solar Maximum Mission coronagraph/polarimeter, *Astrophys. J.*, **244**, L117, 1981.

Howard, R. A., D. J. Michels, N. R. Sheeley Jr., and M. J. Koomen, The observation of a coronal transient directed at earth, *Astrophys. J.*, **263**, L101, 1982.

Howard, R. A., D. Michels, N. R. Sheeley, and M. J. Koomen, Coronal mass ejections—1979-1981, *J. Geophys. Res.*, **90**, 8173, 1985.

Hudson, H. S., Solar flares, microflares, nanoflares, and coronal heating, *Sol. Phys.*, **133**, 357, 1991.

Hudson, H. S. and D. F. Webb, Soft X-ray signatures of coronal ejections, in *Coronal Mass Ejections, AGU Monograph 99*, p. 27, 1997.

Hudson, H. S. and E. W. Cliver, Observing coronal mass ejections without coronagraphs, *J. Geophys. Res.*, **106**, 25199, 2001.

Hudson, H. S., T. Kosugi, N. V. Nitta, and M. Shimojo, Hard X-radiation from a fast coronal ejection, *Astrophys. J.*, **561**, L211, 2001.

Hundhausen, A. J., Sizes and locations of coronal mass ejections—SMM observations from 1980 and 1984-1989, *J. Geophys. Res.*, **98**, 13177, 1993.

Hundhausen, A. J., An introduction, in *Coronal Mass Ejections, AGU Monograph 99*, p.1, 1997.

Hundhausen, A. J., Coronal mass ejections, in *The Many Faces of the Sun*, edited by K. T. Strong, J. L. R. Saba, and B. M. Haisch, p. 143, Springer-Verlag, New York, 1999.

Hundhausen, A. J., J. T. Burkepile, and O. C. St. Cyr, Speeds of coronal mass ejections: SMM observations from 1980 and 1984-1989, *J. Geophys. Res.*, **99**(A4), 6543, 1994.

Illing, R. M. E. and A. J. Hundhausen, Disruption of a coronal streamer by an eruptive prominence and coronal mass ejection, *J. Geophys. Res.*, **91**, 10951, 1986.

Jackman, C. H., N. Achilleos, E. J. Bunce *et al*., Neutral atmospheric influences of the solar proton events in October-November 2003, *J. Geophys. Res.*, **110**, A09S27, 2005.

Kahler, S., The morphological and statistical properties of solar X-ray events with long decay times, *Astrophys. J.*, **214**, 891, 1977.

Kahler, S. W., Injection profiles of solar energetic particles as functions of coronal mass ejection heights, *Astrophys. J.*, **428**, 837, 1994.

Kahler, S. W., The correlation between solar energetic particle peak intensities and speeds of coronal mass ejections: Effects of ambient particle intensities and energy spectra, *J. Geophys. Res.*, **106**, 20947, 2001.

Kahler, S. W., Observational properties of coronal mass ejections, in *Solar Eruptions and Energetic Particles, AGU Monograph 165*, 21, 2006.

Kahler, S. W. and A. Vourlidas, Fast coronal mass ejection environments and the production of solar energetic particle events, *J. Geophys. Res.*, **110**, A12S01, 2005.

Kahler, S. W., E. Hildner, and M. A. I. van Hollebeke, Prompt solar proton events and coronal mass ejections, *Sol. Phys.*, **57**, 429, 1978.

Kamide, Y., N. Yokoyama, W. Gonzalez *et al*., Two-step development of geomagnetic storms, *J. Geophys. Res.*, **103**, 6917, 1998.

Kane, R. P., The idea of Space Weather A historical perspective, *Adv. Space Res.*, **37**, 1261, 2006.

Kay, H. R. M., L. K. Harra, S. A. Matthews, J. L. Culhane, and L. M. Green, The soft X-ray characteristics of solar flares, both with and without associated CMEs, *Astron. Astrophys.*, **400**, 779, 2003.

Koomen, M., R. Howard, R. Hansen, and S. Hansen, The coronal transient of 16 June 1972, *Sol. Phys.*, **34**, 447, 1974.

Kudela, K., M. A. Shea, D. F. Smart, and L. C. Gentile, Relativistic solar particle events recorded by the Lomnicky Stit neutron monitor, *Proc. 1993 ICRC 3*, 71, 1993.

Kunow, H., N. U. Crooker, J. A. Linker, R. Schwenn, and von R. Steiger, *Coronal mass ejections*, Springer, 2006.

Lepping, R. P. and D. Berdichevsky, Interplanetary magnetic clouds: Sources, properties, modeling, and geomagnetic relationship, *Recent. Res. Geophys.*, **3**, 77, 2000.

Lepri, S. T., T. Zurbuchen, L. Fisk, I. Richardson, H. V. Cane, and G. Gloeckler, Iron charge distribution as an identifier of interplanetary coronal mass ejections, *J. Geophys. Res.*, **106**, 29231, 2001.

Li, Y. and J. G. Luhmann, Solar cycle control of the magnetic cloud polarity and the geoeffectiveness, *J. Atmos. Sol.-Terr. Phys.*, **66**, 323, 2004.

Lin, R. P., Solar particle acceleration and propagation, *Rev. Geophys.*, **25**, 676, 1987.

Lindsay, G. M., J. G. Luhmann, C. T. Russell, and J. T. Gosling, Relationships between coronal mass ejection speeds from coronagraph images and interplanetary characteristics of associated interplanetary coronal mass ejections, *J. Geophys. Res.*, **104**, 12515, 1999.

Loewe, C. A. and G. W. Prolss, Classification and mean behavior of magnetic storms, *J. Geophys. Res.*, **102**, 14209, 1997.

Lopate, C., Fifty years of ground level solar particle event observations, in *Solar Eruptions and Energetic Particles, AGU Monograph 165*, 283, 2006.

Lopez, R. E. and J. W. Freeman, Solar wind proton temperature-velocity relationship, *J. Geophys. Res.*, **91**, 1701, 1986.

Lorentzen, K. R., J. E. Mazur, M. D. Looper, J. F. Fennell, and J. B. Blake, Multisatellite observations of MeV ion injections during storms, *J. Geophys. Res.*, **107**(A09), 1231, 2002.

Mann, G., A. Klassen, H. Aurass, and H.-T. Classen, Formation and development of shock waves in the solar corona and the near-Sun interplanetary space, *Astron. Astrophys.*, **400**, 329, 2003.

Mewaldt, R. A., Solar energetic particle composition, energy spectra, and space weather, *Space Sci. Rev.*, **124**, 303, 2006.

Meyer, P., E. N. Parker, and J. A. Simpson, Solar cosmic rays of February, 1956 and their propagation through interplanetary space, *Phys. Rev*, **104**, 768, 1956.

Michalek, G., An asymmetric cone model for halo coronal mass ejections, *Sol. Phys.*, **237**, 101, 2006.

Moon, Y.-J., G. Choe, H. Wang, Y. Park, N. Gopalswamy, G. Yang, and S. Yashiro, A statistical study of two classes of coronal mass ejections, *Astrophys. J.*, **581**, 694, 2002.

Moore, R. L., A. C. Sterling, H. S. Hudson, and J. R. Lemen, Onset of the magnetic explosion in solar flares and coronal mass ejections, *Astrophys. J.*, **552**, 833, 2001.

Moreton, G. E., Hα observations of flare-initiated disturbances with velocities ∼1000 km/sec, *Astron. J.*, **65**, 494, 1960.

Mulligan, T., C. T. Russell, and J. G. Luhmann, Solar cycle evolution of the structure of magnetic clouds in the inner heliosphere, *Geophys. Res. Lett.*, **25**, 2959, 1998.

Munro, R. H., J. T. Gosling, E. Hildner, R. M. MacQueen, A. I. Poland, and C. L. Ross, The association of coronal mass ejection transients with other forms of solar activity, *Sol. Phys.*, **61**, 201, 1979.

Narukage, N., H. S. Hudson, T. Morimoto *et al.*, Simultaneous observation of a Moreton wave on 1997 November 3 in Hα and soft X-rays, *Astrophys. J.*, **572**, L109, 2002.

Nelson, G. J. and D. B. Melrose, Type II bursts, in *Solar radiophysics*, p. 333, Cambridge University Press, New York, 1985.

Neugebauer, M. and B. E. Goldstein, Particle and field signatures of coronal mass ejections in the solar wind, in *Coronal Mass Ejections, AGU Monograph 99*, 245, 1997.

Neugebauer, M., J. T. Steinberg, R. L. Tokar *et al.*, Genesis on-board determination of the solar wind flow regime, *Space Sci. Rev.*, **105**, 661, 2003.

Neupert, W. M., Transient coronal extreme ultraviolet emission before and during the impulsive phase of a solar flare, *Astrophys. J.*, **344**, 504, 1989.

Ohtani, S., M. Nosé, G. Rostoker, H. Singer, A. T. Y Lui, and M. Nakamura, Storm-substorm relationship: Contribution of the tail current to Dst, *J. Geophys. Res.*, **106**, 21199, 2001.

Ohtani, S., P. C. Brandt, D. G. Mitchell *et al*., Storm-substorm relationship: Variations of the hydrogen and oxygen energetic neutral atom intensities during storm-time substorms, *J. Geophys. Res.*, **110**, A07219, 10.1029/2004JA010954, 2005.

Ohtani, S., H. Korth, P. C. Brandt *et al*., Cluster observations in the inner magnetosphere during the 18 April 2002 sawtooth event: Dipolarization and injection at r = 4.6 RE, *J. Geophys. Res.*, **112**, A08213, doi:10.1029/2007JA012357, 2007.

Parker, E. N., The gross dynamics of a hydromagnetic gas cloud, *Astrophys. J.*, **S 3**, 51, 1957.

Reames, D., Particle acceleration at the Sun and in the heliosphere, *Space Sci. Rev.*, **90**, 413, 1999.

Reinard, A. A., Comparison of interplanetary CME charge state composition with CME-associated flare magnitude, *Astrophys. J.*, **620**, 501, 2005.

Riley, P., C. Schatzman, H. V. Cane, I. G. Richardson, and N. Gopalswamy, On the rates of coronal mass ejections: Remote solar and in situ observations, *Astrophys. J.*, **647**, 648, 2006.

Rust, D. M., Coronal disturbances and their terrestrial effects /Tutorial Lecture/, *Space Sci. Rev.*, **34**, 21, 1983.

Sheeley, N. R., W. N. Hakala, and Y.-M. Wang, Detection of coronal mass ejection associated shock waves in the outer corona, *J. Geophys. Res.*, **105**, 5081, 2000.

Shibata, K., S. Masuda, M. Shimojo *et al*., Hot-plasma ejections associated with compact-loop solar flares, *Astrophys. J.*, **451**, L83, 1995.

Song, P., H. J. Singer, and G. L. Siscoe, Space weather, *AGU Monograph 125*, 2001.

Švestka, Z. and E. W. Cliver, History and basic characteristics of eruptive flares, in *Eruptive Solar Flares*, edited by Z. Švestka, B. V. Jackson and M. E. Machado, p. 1, Springer, New York, 1992.

Tandberg-Hanssen, E., *The Nature of Solar Prominences*, Kluwer, Dordrecht, 1995.

Thompson, B. J., J. Gurman, W. Neupert *et al*., SOHO/EIT observations of the 1997 April 7 coronal transient: Possible evidence of coronal Moreton waves, *Astrophys. J.*, **517**, L151, 1999.

Thompson, B. J., E. W. Cliver, N. Nitta, C. Delannée, and J.-P. Delaboudiniére, Coronal dimmings and energetic CMEs in April-May 1998, *Geophys. Res. Lett.*, **27**, 1431, 2000.

Tokumaru, M., M. Kojima, K. Fujiki, M. Yamashita, and B. V. Jackson, The source and propagation of the interplanetary disturbance associated with the full-halo coronal mass ejection on 28 October 2003, *J. Geophys. Res.*, **112**, A05106, 2007.

Tripathi, D., V. Bothmer, and H. Cremades, The basic characteristics of EUV post-eruptive arcades and their role as tracers of coronal mass ejection source regions, *Astron. Astrophys.*, **422**, 337, 2004.

Tsurutani, B. T., E. J. Smith, W. D. Gonzalez, F. Tang, and S.-I. Akasofu, Origin of interplanetary southward magnetic fields responsible for major magnetic storms near solar maximum (1978-1979), *J. Geophys. Res.*, **93**, 8519, 1988.

Turner, R. E., Space weather challenges intrinsic to the human exploration of space, in *Solar Eruptions and Energetic Particles, AGU Monograph 165*, 367, 2006.

Tylka, A. J., C. M. S Cohen, W. F. Dietrich *et al*., Shock geometry, seed populations, and the origin of variable elemental composition at high energies in large gradual solar particle events, *Astrophys. J.*, **625**, 474, 2005.

Uchida, Y., On the exciters of type II and type III solar radio bursts, *PASJ*, **12**, 376, 1960.

Vennerstroem, S., Interplanetary sources of magnetic storms: A statistical study, *J. Geophys. Res.*, **106**, 29175, 2001.

Veronig, A., M. Temmer, B. Vršnak, and J. Thalmann, Interaction of a Moreton/EIT wave and a coronal hole, *Astrophys. J.*, **647**, 1466, 2006.

Vourlidas, A., D. Buzasi, R. A. Howard, and E. Esfandiari, Mass and energy properties of LASCO CMEs, in *Solar variability: from core to outer frontiers*, edited by A. Wilson, ESA SP-506, Vol. 1, Noordwijk: ESA Publications Division, p. 91, 2002.

Vourlidas, A., S. T. Wu, A. H. Wang, P. Subramanian, and R. A. Howard, Direct detection of a coronal mass ejection-associated shock in large angle and spectrometric coronagraph experiment white-light images, *Astrophys. J.*, **598**, 1392, 2003.

Vršnak, B., D. Ruzdjak, D. Sudar, and N. Gopalswamy, Kinematics of coronal mass ejections between 2 and 30 solar radii. What can be learned about forces governing the eruption?, *Astron. Astrophys.*, **423**, 717, 2004.

Vršnak, B., D. Sudar, and D. Ruzdjak, The CME-flare relationship: Are there really two types of CMEs?, *Astron. Astrophys.*, **435**, 1149, 2005.

Wang, C., D. Du, and J. D. Richardson, Characteristics of the interplanetary coronal mass ejections in the heliosphere between 0.3 and 5.4 AU, *J. Geophys. Res.*, **110**, A10107, 2005.

Warmuth, A., B. Vršnak, H. Aurass, and A. Hanslmeier, Moreton waves and their relation with EIT waves, in *Proceedings of the Second Solar Cycle and Space Weather Euroconference*, *ESA SP 477*, 195, 2002.

Webb, D. F., E. W. Cliver, N. U. Crooker, O. C. St. Cyr, and B. J. Thompson, Relationship of halo coronal mass ejections, magnetic clouds, and magnetic storms, *J. Geophys. Res.*, **105**, 7491, 2000.

Wild, J. P. and S. F. Smerd, Radio bursts from the solar corona, *Ann. Rev. Astron. Astrophys.*, **10**, 159, 1972.

Xie, H., L. Ofman, and G. Lawrence, Cone model for halo CMEs: Application to space weather forecasting, *J. Geophys. Res.*, **109**, 3109, 2004.

Yashiro, S., N. Gopalswamy, G. Michalek *et al.*, A catalog of white light coronal mass ejections observed by the SOHO spacecraft, *J. Geophys. Res.*, **109**, A07105, 2004.

Yashiro, S., S. Akiyama, N. Gopalswamy, and R. A. Howard, Different power-law indices in the frequency distributions of flares with and without coronal mass ejections, *Astrophys. J.*, **650**, L143, 2006.

Yashiro, S., G. Michalek, S. Akiyama, N. Gopalswamy, and R. A. Howard, Spatial relationship between solar flares and coronal mass ejections, *Astrophys. J.*, **673**, 1174, 2008a.

Yashiro, S., G. Michalek, and N. Gopalswamy, A comparison of coronal mass ejections identified by manual and automatic methods, *Ann. Geophys.*, **26**, 3103, 2008b.

Yeh, C.-T., M. D. Ding, and P. F. Chen, Kinetic properties of CMEs corrected for the projection effect, *Sol. Phys.*, **229**, 313, 2005.

Yurchyshyn, V., Relationship between EIT posteruption arcades, coronal mass ejections, the coronal neutral line, and magnetic clouds, *Astrophys. J.*, **675**, L49, 2008.

Yurchyshyn, V., H. Wang, P. R. Goode, and Y. Deng, Orientation of the magnetic fields in interplanetary flux ropes and solar filaments, *Astrophys. J.*, **563**, 381, 2001.

Zarro, D., A. C. Sterling, B. J. Thompson, H. S. Hudson, and N. Nitta, SOHO EIT observations of extreme-ultraviolet "dimming" associated with a halo coronal mass ejection, *Astrophys. J.*, **520**, L193, 1999.

Zhang, J., K. P. Dere, R. A. Howard, M. R. Kundu, and S. M. White, On the temporal relationship between coronal mass ejections and flares, *Astrophys. J.*, **559**, 452, 2001.

Zhang, J., I. Richardson, D. F. Webb *et al.*, Solar and interplanetary sources of major geomagnetic storms (Dst ≤ -100 nT) During 1996–2005, *J. Geophys. Res.*, **112**, A10102, 2007.

Zhao, X. P., Inversion solutions of the elliptic cone model for disk frontside full halo coronal mass ejections, *J. Geophys. Res.*, **113**, A02101, 2008.

Zhao, X. P. and D. F. Webb, Source regions and storm effectiveness of frontside full halo coronal mass ejections, *J. Geophys. Res.*, **108**(A6), 1234, 2003.